Cavitation underwater radiated noise methodology applied to a propeller operating in-behind condition

Ocean Engineering 349 (2026) 124084

Contents lists available at ScienceDirect

Ocean Engineering

journal homepage: www.elsevier.com/locate/oceaneng

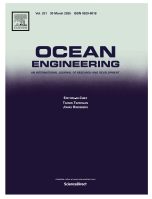

Research paper

Cavitation underwater radiated noise methodology applied to a propeller operating in-behind condition

Qais Shehadeh Khraisat [a,*], Martin Persson [b], Rickard E. Bensow [a]

[a] Department of Mechanics and Maritime Sciences, Chalmers University of Technology, Chalmersplatsen 4, Gothenburg, 412 96, Sweden
[b] Kongsberg Hydrodynamic Research Center, Kristinehamn, 68193, Sweden

ARTICLE INFO

Keywords:
Pressure pulses
Underwater radiated noise
Cavitating propeller
Full scale
Model scale
Acoustic analogy
Blockage effects

ABSTRACT

Concerns about shipping noise influence on marine life are motivating mitigation efforts, increasing interest in numerical methods for underwater radiated noise (URN) assessment. A common approach is to use incompressible flow solvers with the Ffowcs Williams-Hawkings (FW-H) method, though reliability is shown to depend on modelling choices.

To advance on this matter, model and full scale simulations are performed for a fully appended ship, operating in mildly cavitating conditions, using the incompressible Reynolds-averaged Navier–Stokes (RANS) framework to investigate pressure pulse and URN levels. Predictions are compared with model scale experiments and full scale sea trial measurements. The permeable FW-H method is used, while also an alternative approach modelling cavitation as a monopole source combined with the solid FW-H formulation and corrections for Lloyd's mirror effect is proposed and tested.

Further, the effect of blockage on cavitation is investigated and found to affect induced pressure pulse and URN levels due to effects on the ship wakefield in the tunnel section. Although good agreement is found for cavity dynamics and pressure pulses, significant discrepancies are found in URN levels between measurements and numerical predictions, for both methods. Reasons for these differences are partly understood and discussed, while other questions remain open.

1. Introduction

Growing concerns over the increasing levels of underwater radiated noise (URN) from merchant shipping have gained increased attention within the maritime community. Efforts to regulate and reduce noise levels are driven by the potential negative impact on the well-being of marine animals. Given indications of global trends and the overlap between ship noise emissions and the hearing ranges of marine animals, concerns have been raised about the potential dangers. The review by Duarte et al. (2021) find that almost all studies performed on how anthropogenic noise, including shipping noise, affect marine wildlife show a negative effect. In addition, noise levels from the shipping industry are continuously rising, as trends indicate an average increase of 3.3 dB per decade (Frisk, 2012). A recent study further supports these trends, predicting that noise emissions will double every 11.5 years (Jalkanen et al., 2022). Energy input to the ocean, which includes sound, was acknowledged as a pollutant by the EU in 2008 within the Marine Strategy Framework Directive (MSFD) (Directive, 2008). Recently, an assessment framework that included threshold values for anthropogenic noise was adopted by the EU, forming a basis for future regional and national regulations (Borsani et al., 2023). In 2014, the International Maritime Organization (IMO) recognized underwater radiated noise from ships as an environmental threat and proposed guidelines to mitigate its effects (Organization, 2014). A revised report was published (Organization, 2023) providing recommendations on design considerations, on-board machinery, maintenance, and operational decisions. However, how general and effective these recommendations are is still a matter for investigations. Regulations and standards are continuously being developed targeting the standardization of underwater acoustic terminology (ISO 18405:2017, 2017) as well as ship scale noise measurements in deep waters (ISO 17208-1:2016, 2016).

Driven by these environmental concerns and regulations, efforts are needed to develop reliable prediction methods for URN from ships in order to find effective measures during the design phase of a vessel or to make decisions for retrofits. Thus, the goal is to obtain accurate full scale underwater radiated noise signatures through model scale tests and numerical prediction methods. In addition, sea trial measurements are important for establishing best practices and for developing and verifying prediction methods in both model tests and numerical predictions.

* Corresponding author.
E-mail addresses: qais.khraisat@chalmers.se (Q.S. Khraisat), rickard.bensow@chalmers.se (R.E. Bensow).

https://doi.org/10.1016/j.oceaneng.2025.124084
Received 4 November 2025; Received in revised form 15 December 2025; Accepted 22 December 2025
Available online 9 January 2026

One of the earliest efforts aimed at the assessment of URN and the validation of scaling laws is presented by Bark (1985) through the comparison of model and full scale noise measurements. Discrepancies were found in the noise signature when the scaling procedure was applied, but were partially attributed to uncertainties related to cavitation intermittency, calibration challenges, and acoustic wave reflections and scattering. The outcomes of this study were later used to develop ITTC noise scaling recommendations and guideline procedures.

Although available data on underwater radiated noise from sea trials remain limited, more recent studies have been published investigating URN at model and full scale conditions. Aktas et al. (2016) investigated URN from a cavitating propeller mounted behind a dummy hull in a tunnel section and compared results with full scale measurements. The results showed that the extrapolated levels using the ITTC scaling procedure agrees reasonably well at low frequencies, but larger differences are observed at higher frequencies. Lafeber et al. (2017) presented full scale URN measurements and compared with model tests at a depressurized wave basin for a controllable pitch propeller at different pitch settings. Reasonable agreement across different pitch settings was found, although the unstable sheet cavitation in the model tests influenced the low frequency noise levels. Li et al. (2018) compared predicted noise levels from numerical simulations, model scale tests, and sea trial measurements. The results showed 7 dB difference in source level for the Blade Pass Frequency (BPF) tones between the measurements and even larger discrepancies were found at higher frequencies. These studies highlight the challenges associated with obtaining accurate URN predictions when comparing model tests to full scale sea trials and the need for future investigations.

Model scale tests are commonly used to obtain underwater radiated noise level predictions. They are however influenced by uncertainties related to scale effects, background noise, acoustic reverberation, water nuclei and air content, and the accuracy of wakefield distribution (Tani et al., 2020). One of the main limitations of cavitation tunnels in the context of noise assessment is the reverberations that lead to acoustic interferences and transfer functions must be determined to correct for that effect (Tani et al., 2019). The ITTC (ITTC 7.5-02-03-03.9, 2024) continuously updates correction procedures and guidelines to mitigate some of these uncertainties, but no fully reliable procedure is yet available. For example, Tani et al. (2020) presented a study for a measurement campaign on underwater radiated noise where seven institutes participated. Although cavitation patterns between the facilities are within reasonable agreement, large discrepancies in the noise levels is reported, on the order of up to 20 dB.

Besides the acoustical considerations, the interaction between the ship model and tunnel walls affects flow field dynamics and pressure distribution, a phenomenon referred to as blockage. While blockage is studied in other research communities (Fischer et al., 2010; Meng et al., 2020; Espina-Valdés et al., 2020), there is a lack of understanding for its effects on cavitation within the maritime community. Recent work by Katsuno and Dantas (2022) investigated the influence of small tunnels on propellers operating in uniform inflow conditions and found that the cavitation extent is indeed sensitive to blockage. While ITTC (ITTC 7.5-02-03-03.9, 2024) recommends maintaining blockage below 20%, this is a practical recommendation (in most windtunnels a blockage above 5% is deemed unacceptable) and it is not well understood how it affects performance, cavitation dynamics, pressure pulse and noise levels when the propeller is operating in-behind hull conditions.

Several numerical prediction methods for underwater radiated noise from ships have been proposed with varying complexity and computational requirements. The Direct Method is the most computationally demanding, as noise sources and acoustic waves need to be captured using compressible approaches with a resolution that allows accurate wave propagation through the domain. In contrast, semi-empirical methods provide a more cost-effective approach for URN predictions (Bosschers, 2017). While semi-empirical methods are useful for obtaining preliminary estimates, their accuracy is limited. What is often called the hybrid approach, developed within computational aeroacoustics, offers a balance between robustness and computational efficiency as the sound propagation problem is decoupled from the flow computations. With this method, the flow fields and sound sources are modelled using Computational Fluid Dynamics (CFD), and the far-field acoustic propagation is computed with an acoustic analogy. The Ffowcs Williams-Hawkings (FW-H) (Ffowcs Williams and Hawkings, 1969) acoustic analogy is now widely adopted within the maritime community. However, the FW-H method was developed for compressible single-phase flows and the theoretical basis for its use together with incompressible multiphase flow solvers, a necessity for ship applications, is still not clarified.

Several studies on non-cavitating propeller noise emission computed with FW-H acoustic analogy have been reported over the last decade. Ianniello et al. (2013) investigated the application of the FW-H acoustic analogy for marine propellers in open water using an incompressible RANS approach. The hydrodynamic loads were satisfactorily captured, indicating accurate prediction of thickness and loading acoustic terms. However, the quadrupole sources (vorticity and turbulence) were found to be underpredicted with the RANS approach. They argued that for such low Mach applications, the incompressibility approximation is practically acceptable as the time shift between acoustic sources is negligible but that for marine propellers the quadropole sources need to be considered. These claims were disputed by Ahmed (2020) who used various FW-H configurations for compressible and incompressible CFD for a non-cavitating marine propeller and compared with direct computation of the sound propagation. He reported erroneous URN predictions when the FW-H approach was combined with an incompressible flow input, especially when using permeable data surfaces, presuambly due to the lack of correct wave propagation in the near field. However, not considering the quadrapole sources did not lead to significant errors. Later studies, e.g. Cianferra et al. (2019), Keller et al. (2018), Posa et al. (2023), have used the FW-H method to study the hydroacoustics of a marine propeller in non-cavitating operation, however without comparisons made with direct computations or physical experiments.

One of the earliest applications of the FW-H acoustic analogy for cavitating propellers is presented by Salvatore and Ianniello (2003). Predictions with this approach are compared with a potential flow method. Although discrepancies were reported, the FW-H acoustic analogy successfully captured the noise signature induced by cavitation. More recently, Ge et al. (2020) show that viscous CFD can satisfactorily predict large-scale cavitation dynamics but smaller or vortical structures are typically underpredicted. This is mainly attributed to the underprediction of dynamic wakefield and the transient flow characteristics interacting with the propeller blades (Bensow, 2015; Bensow and Liefvendahl, 2016) as well as the diffusive characteristic of the RANS approach (Ge et al., 2020). However, even when using scale-resolving frameworks for propeller simulations, challenges remain in fully resolving cavitating tip vortex dynamics due to the high spatial resolution requirements (Li et al., 2018). Further studies have increasingly focused on the application of the permeable Ffowcs Williams-Hawkings (FW-H) approach for predicting underwater radiated noise from cavitating propellers (Lidtke et al., 2022; Sezen and Atlar, 2023; Kimmerl and Abdel-Maksoud, 2023). In addition, best practices for applying this approach to underwater acoustics are still under development, with some recommendations are proposed by Testa et al. (2021).

This is despite that the permeable FW-H approach has been reported to produce erroneous results in certain circumstances. Ge et al. (2022) described several issue when using an incompressible flow input in combination with the permeable FW-H, primarily in higher frequencies although the whole frequency range is affected. The reasons were related to both phase errors inside the permeable surface as well as the missing velocity perturbations from the propagating waves. The studies were extended by Vikström et al. (2022) regarding the shape and size of the permeable data surface (PDS). It was reported that spherical surfaces with the sound source in the center could be used without excessive errors. An attempt to avoid the permeable FW-H and use an efficient

method for direct integration considering also the multiphase aspect of the problem has been presented by Wang et al. (2022), but it's applicability for realistic flow cases needs to be further investigated.

Given the limitations associated with the permeable FW-H, this paper develops an alternative approach to predict underwater radiated noise from cavitating propellers, based on the ideas introduced by Ge et al. (2022). The proposed approach models cavitation-induced underwater radiated noise as a pulsating monopole source in combination with the solid FW-H formulation, and including correction for free surface reflections. Furthermore, we extend the existing literature on the limitations of the permeable FW-H with incompressible flow input with an investigation on PDS size, receiver placement, and the end-cap effect on predicted URN levels. The influence of tunnel size (blockage) on cavitation dynamics, pressure pulses, and underwater radiated noise levels is also presented. Pressure pulse and URN levels are compared with sea trials and cavitation tunnel model scale tests.

2. Methodologies for predicting underwater radiated noise

Although previous studies, as discussed in Section 1, have highlighted the issues and limitations associated with the FW-H acoustic analogy in hydroacoustic applications, it is still used in this paper. In addition, we propose an alternative approach that could potentially bypass some of these issues.

2.1. Ffowcs Williams and Hawkings (FW-H) acoustic analogy

The Ffowcs Williams and Hawkings (FW-H) method (Ffowcs Williams and Hawkings, 1969) extends Lighthill's and Curle's analogies (Lighthill, 1954; Curle, 1955) to predict far-field sound generated by moving surfaces. The basic idea is to reformulate the propagation problem in an unbound domain to an integral problem over the sound sources. The approach uses generalized derivatives and a Heaviside function H_s to define the surfaces, and by applying the method of Green's function, the solution to the inhomogeneous wave equation in a free field medium is,

$$P'(x,t)H_s = P'_T(x,t) + P'_L(x,t) + P'_Q(x,t). \tag{1}$$

In this equation, $P'_T(x,t)$ is the thickness term accounting for the monopole contributions,

$$P'_T(x,t) = \frac{1}{4\pi}\frac{\partial}{\partial t}\int_S \left[\frac{(\rho U_i - \rho' V_i)n_i}{|1-M_r|r}\right]_{ret}, \tag{2}$$

where U represents the velocity of the fluid medium, V is the velocity of the moving surface, n is a unit normal to the surface, M_r is the relative Mach number, and r is the distance between the source and receiver. The subscript *ret* indicates that the integral sources should be evaluated at a retarded time. The thickness term describes the noise generated due to the mass flux across a surface which would reduce to zero for impermeable surfaces.

$P'_L(x,t)$ is the loading term accounting for the dipole contributions,

$$P'_L(x,t) = \frac{1}{4\pi}\frac{\partial}{\partial x_i}\int_S \left[\frac{(\rho U_j(U_i - V_i) + P_{ij})n_i}{|1-M_r|r}\right]_{ret}. \tag{3}$$

Here P_{ij} is the compressive stress tensor, mainly accounting for the dominant pressure forces. The term $\rho U_i U_j$ also reduces to zero for impermeable surfaces.

Finally, $P'_Q(x,t)$ represents the quadrupole term which accounts for the sound generated by flow structures,

$$P'_Q(x,t) = \frac{1}{4\pi}\frac{\partial^2}{\partial x_i x_j}\int_V \left[\frac{T_{ij}}{|1-M_r|r}\right]_{ret}, \tag{4}$$

where, T_{ij} is the Lighthill stress tensor which is defined as $T_{ij} = \rho u_i u_j + P_{ij} - c^2(\rho - \rho_\infty)\delta_{ij}$, where c is the speed of sound.

The Farasat 1A formulation (Farassat, 2007) of the FW-H acoustic analogy is used in this work as it is suitable for subsonic source regions. Since cavitation is a volume source, a Permeable Data Surface (PDS) is required in combination with the FW-H acoustic analogy to account for its noise emissions. Note however that this formulation was developed for single-phase flows. An extension to turbulent two-phase flow without mass transfer is discussed by Crighton and Ffowcs Williams (1969), but the use in cavitating flows has not been theoretically investigated despite the extensive use in literature. More details on the PDS configuration and receivers placement are provided in Section 4.2.

2.2. Cavitation as monopole source

The noise generated from cavitation primarily radiates as a monopole source. An early study on cavitation noise propagation as a monopole source is presented by Gray and Greeley (1978) and later further explored by Arveson and Vendittis (2000). Given that cavitation dominates other noise mechanisms, the proposed methodology focuses on the prediction of its underwater radiated noise levels. The instantaneous radiated acoustic pressure in free-field conditions for a monopole source of fluctuating volume is derived by solving the wave equation,

$$\nabla^2 p = \frac{1}{c^2}\frac{\partial^2 p}{dt^2}, \tag{5}$$

where p is the acoustic pressure and c is the speed of sound in a given medium. For spherical wavefronts, where pressure is assumed to be uniform over a spherical surface, the solution to the wave equation in spherical coordinates is,

$$p(r,t) = \frac{1}{r}f(ct-r) + \frac{1}{r}g(ct+r). \tag{6}$$

Here, r represents the distance of the radiated acoustic wave from the source, f is the solution to a forward-moving wave and g is a backward (reflected) wave. Assuming harmonic time dependence and neglecting the reflected waves, the solution to the simplified expression for a pulsating monopole source becomes,

$$p(t) = \frac{\rho}{4\pi r}\ddot{V}(t), \tag{7}$$

where $\ddot{V}(t)$ is the second-order derivative of the source volume. For more details on the derivation, please refer to William (2017). It is important to emphasize that the final expression given in Eq. (7) is derived based on the following assumptions:

- The wavefronts are assumed to be spherical with pressure being uniform over a spherical surface.
- Reflected waves are neglected and only forward-propagating waves are considered.
- The diameter of the spherical source is assumed to be much smaller than the acoustic wavelength.
- The diameter of the spherical source is assumed to be significantly smaller than the radial distance, which is valid for far-field predictions.

One of the key limitations in treating cavitation as a monopole source, as well as in the FW-H acoustic analogy, is the assumption of free-field propagation. In the context of underwater acoustics, this assumption is invalid due to phenomena related to reflections and scattering on the hull, sea surface and seabed. The Lloyd mirror in particular describes the influence of reflected waves from the sea surface on the perceived radiated noise levels. A spatially dependent constructive and destructive interference pattern will occur between the direct and reflected acoustic waves. In this work, the source level is computed by applying corrections for the propagation losses PL_{LM} following ISO 17208-2 (2019),

$$P_{L_{LM}} = \begin{cases} -10\log_{10}\left[4\sin^2\left(kd_s\sin\theta\right)\right], & kd_s\sin\theta \le \frac{3\pi}{4} \\ -10\log_{10}[2], & kd_s\sin\theta > \frac{3\pi}{4} \end{cases}$$

here, d_s is the source depth assumed to be at 0.9R of the propeller radius, k is the acoustic wave number, and θ is the depression angle of the hydrophone.

2.3. Sound spectra computation

The power spectral density ϕ_{pp} is computed by applying FFT to the acoustic pressure signal, which is then used to calculate the Sound Pressure Spectral Density Level (SPL) defined as,

$$SPL(f,\Delta f) = 10\log_{10}\left(\frac{\phi_{pp}(f,\Delta f)}{p_{ref}^2}\right), \tag{8}$$

where f is the frequency, p_{ref} is the reference pressure set at 1μ Pa, and the unit of SPL is dB *re* $1\mu\text{Pa}^2$/Hz. The Radiated Noise Level (RNL) is defined by correcting the measured SPL at the corresponding hydrophone locations and applying distance normalization correction assuming spherical spreading loss which is expressed as,

$$RNL = SPL(f,\Delta f) + 20\log_{10}\left(\frac{r}{r_{ref}}\right), \tag{9}$$

where r is the distance from the hydrophone to the acoustic center and r_{ref} is the reference distance set at 1.0 m.

A scaling procedure following ITTC recommendations (ITTC 7.5-02-03-03.9, 2024) is applied to the model scale RNL to compare with full scale predictions. The frequency spectrum is scaled with the following relation,

$$\frac{f_s}{f_m} = \frac{n_s}{n_m}\sqrt{\frac{\sigma_s}{\sigma_m}}. \tag{10}$$

Here, subscripts m and s refer to model and full scale conditions, while σ is the cavitation number. Scaling the Sound Pressure Level for proportional bandwidth (1/3 octave bands) is given by,

$$\Delta SPL = 20\log_{10}\left[\left(\frac{\sigma_s}{\sigma_m}\right)^w\left(\frac{r_m}{r_s}\right)^x\left(\frac{n_s D_s}{n_m D_m}\right)^y\left(\frac{D_s}{D_m}\right)^z\right], \tag{11}$$

where exponents w, x, y, z are constants and their values depend on high and low frequency cut off criterion which assumed to be at 2000 Hz.

3. Case description

A moderately skewed, controllable-pitch, four-bladed propeller is mounted behind the hull of a chemical tanker. The main geometrical features and characteristics of the ship, including the propeller, are summarized in Table 1.

Sea trials for pressure pulse and underwater radiated noise measurements were performed by Kongsberg Maritime and the Swedish Environmental Research Institute (IVL), respectively, as reported by Andersson et al. (2024). The measurements were carried out approximately 1.7 km southwest of Vinga Island, Gothenburg. Sea depth in this location is approximately 40 m, with the seafloor properties such that it is more or less acoustically transparent. During the measurement phase, the propeller pitch was reduced by the crew, leading to an off-design operating point. As result, the propeller was unloaded and lower levels of cavitation than expected developed. In addition, the ship operated at a slightly reduced speed during the tests in order to be able to keep constant speed during the passages for the URN measurement. Two PCB 112A22 pressure transducers, named Ahead and Astern, were mounted in the hull and above the propeller to measure the pressure pulse levels. Both transducers were positioned 190 mm to the starboard side of the ship's centerline.

Table 1
Ship geometrical features and dimensions at full scale.

	Ship Data
Length between perpendiculars, Lpp	144.3 m
Ship draught, T	8.7 m
Number of propellers	1
Number of blades, Z	4
Direction of rotation	Left hand
Propeller diameter, D	5.7 m
Blade area ratio, A_E/A_O	0.376
Design pitch ratio, P/D	0.978
Blade tip clearance	0.28 × D
Chord length 0.75R	1.25 m

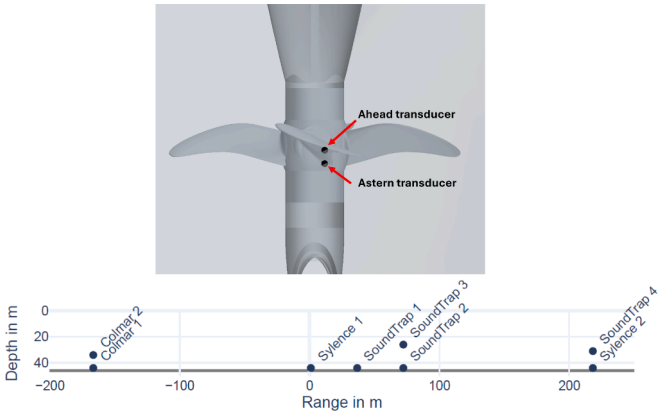

Fig. 1. Ahead and Astern pressure transducers placement during the sea trials (top). Hydrophones placement during the sea trial measurements (bottom).

The Ahead transducer was mounted 95 mm downstream of the propeller plane, while the Astern one was positioned 350 mm downstream. For the underwater radiated noise measurements, eight hydrophones were deployed and their configuration is shown in Fig. 1 (bottom). An attempt was made to do also cavitation observations during the sea trials but the turbidity was too high. Additionally, propagation loss measurements were performed on a separate day. It was reported that favorable calm sea and wind conditions were present during both measurement days. For more details on the sea trial measurements, please refer to Andersson et al. (2024).

Model scale pressure pulse and noise level measurements were performed by RISE in their cavitation tunnel following ITTC recommended procedures and guidelines for model scale cavitation tests. The model was placed in tunnel section 3 that has dimensions of 8.0 m in length, 2.10 m in width, and 1.22 m in height. The hull draft was increased relative to the ship scale fully loaded design condition to compensate for wall effects of the tunnel roof. The tunnel pressure is regulated to achieve the desired cavitation number, based on the static pressure measurement at the propeller shaft centerline. To achieve non-dimensional similarity of thrust and torque coefficients, the propeller rotation rate was adjusted during the tests. It should be noted that a slight mismatch exists between the loading conditions at both scales due to operational limitations at the model scale tests.

Cavitation pattern and behavior was captured using camera recordings with frame rate synchronized to the shaft rotational frequency. Induced pressure pulse fluctuations were measured using eight piezoelectric pressure sensors, and their configuration is shown from a top-view perspective in Fig. 2. Noise level measurements were obtained using three hydrophones positioned near the propeller on the port and starboard sides of the ship. Hydrophones 1 and 2 were located on the port side and positioned 0.41 m and 0.188 m from the acoustic center, respectively. Hydrophone 3 was on the starboard side and placed 0.276 m

Fig. 2. Ship mounting in the cavitation tunnel (left) and top view for the pressure transducers placement during the model tests.

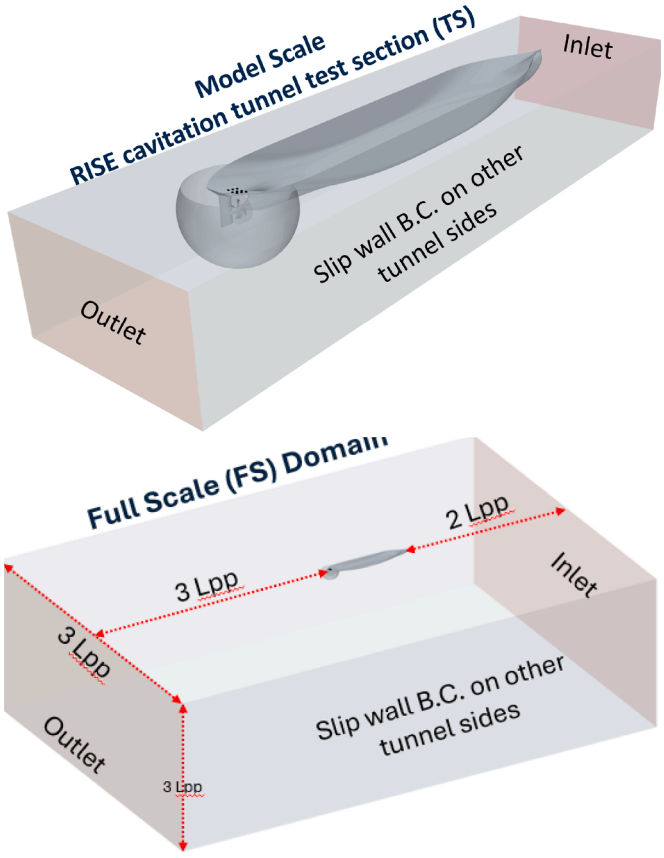

Fig. 3. Computational domains for model scale tunnel section (TS) that is sized to match the RISE cavitation tunnel (top), and full-scale domain designed to mimic open waters condition (bottom).

from the acoustic center. The acoustic center is assumed to be located 0.9R at the 12 o'clock position of the propeller blade.

Model and full scale numerical simulations are performed based on sea trials and experimental operating conditions. The propeller rotation rate is fixed, while the inlet velocity is adjusted to achieve thrust coefficient K_T similarity. The computational domain dimensions at model scale are set to match the RISE cavitation tunnel, while the full scale domain is extended based on ship $L_{pp} = 144.3$ m to simulate free-field conditions and mitigate the effect of walls on the solution. As shown in Fig. 3 (bottom), the inlet is extended $2L_{pp}$ from the bow, $3L_{pp}$ from the stern, and the domain total depth and width are also set to $3L_{pp}$.

To assess blockage effects due to the confined space of the tunnel section, an additional simulation at model scale is performed using a large domain that extends the inlet, outlet, sides, and bottom boundaries. In this work, the tunnel section and large domain are abbreviated with TS and LD, respectively. Due to the change in the tunnel size, the inlet velocity at the LD condition is adjusted while keeping a fixed rotation rate to achieve similarity in propeller loading. A summary of the operational conditions are given in Table 2.

Table 2
Propeller loading conditions at model and full scale conditions.

	K_T	K_Q	σ
CFD MS (TS)	0.145	0.0209	9.43
CFD MS (LD)	0.142	0.0208	9.43
Exp. RISE	0.145	0.0208	9.43
CFD FS	0.158	0.0224	9.46
Sea trial	–	0.0221	9.46

4. Numerical approach

All simulations are performed with the commercial software package Simcenter STAR-CCM+. Cavitation is modeled using the single fluid approach by treating the liquid and vapor phases as one homogeneous mixture. The fluid is assumed to be incompressible with the mixture density varying based on the local volume fraction of vapor α_v. The continuity and momentum equations are solved for the mixture rather than for phases separately. The mixture density and dynamic viscosity μ are defined as,

$$\rho_m = \alpha_v \rho_v + (1 - \alpha_v)\rho_l, \tag{12}$$

$$\mu_m = \alpha_v \mu_v + (1 - \alpha_v)\mu_l. \tag{13}$$

Here subscripts m, v, and l denote mixture, vapor, and liquid, respectively. An additional transport equation is required to solve for the volume fraction α_v,

$$\frac{\partial \alpha_v}{\partial t} + \nabla(\alpha_v u) = \frac{\dot{m}}{\rho}, \tag{14}$$

where $\dot{m}$ represents the mass transfer rate source term for vaporization and condensation. The Schnerr-Sauer mass transfer model is used (Schnerr and Sauer, 2001), and the local volume fraction α_v is defined as the ratio between the local vapor volume and the cell volume,

$$\alpha_v = \frac{V_v}{V_{cell}} = \frac{n_0 \frac{4}{3}\pi R^3}{1 + n_0 \frac{4}{3}\pi R^3}, \tag{15}$$

where n_0 is the initial number of bubbles per unit volume of liquid and R is the bubble radius. All bubbles are initially assumed to be equal in size. The rate of change in the volume fraction is given by,

$$\frac{d\alpha_v}{dt} = \alpha_v(1 - \alpha_v)\frac{3}{R}\frac{dR}{dt}. \tag{16}$$

Effects of bubble acceleration, viscous forces, surface tension, and velocity slip between vapor bubbles and the liquid are neglected. The resulting rate of change for bubble growth and collapse is reduced to,

$$\frac{dR}{dt} = -\text{sign}(P(R) - P_\infty)\sqrt{\frac{2}{3}\frac{|P(R) - P_\infty|}{\rho_l}}, \tag{17}$$

where, $P(R)$ is the bubble internal pressure and P_∞ is the far-field pressure. The mass transfer source term for vaporization and condensation is,

$$\dot{m} = \begin{cases} C_c \frac{\rho_l \rho_v}{\rho_m}\frac{d\alpha_v}{dt}, & \text{if } P(R) > P_v, \\ C_v \frac{\rho_l \rho_v}{\rho_m}\frac{d\alpha_v}{dt}, & \text{if } P(R) \le P_v. \end{cases} \tag{18}$$

The condensation C_c and vaporization C_v coefficients are set to 1.0, while the initial number of bubbles per unit volume of liquid n_0 and diameter are set 10^{12} m^{-3} and 10^{-6} m, respectively.

The Reynolds-averaged Navier-Stokes (RANS) approach is used in the simulations. Mass and momentum equations for the mixture are defined as,

$$\frac{\partial(\rho_m)}{\partial t} + \nabla \cdot (\rho_m U) = 0, \tag{19}$$

$$\frac{\partial(\rho_m U)}{\partial t} + \nabla(\rho_m UU) = -\nabla p + \nabla(\tau - \rho_m \overline{u'u'}) + f. \tag{20}$$

Here, U is the average velocity, p is the pressure, τ is the viscous stress tensor, f is body forces, and $-\rho_m \overline{u'u'}$ is the Reynolds stress tensor. The Boussinesq approximation is extended to consider turbulence anisotropy with a Quadratic Constitutive Relation (QCR). The modification introduces non-linear functions of the strain and vorticity-rate tensors (Spalart, 2000). The added computational cost of the additional gradients is insignificant.

Eddy viscosity is modeled with the $k-\omega$ SST (Menter et al., 2003) which uses the strain rate S to calculate the eddy viscosity μ_T,

$$\mu_T = \frac{\rho k}{\min(\frac{a^*}{\omega}, \frac{a_1}{SF_2})}, \tag{21}$$

where a_1 and a^* are model constants, k is the turbulent kinetic energy, ω is the specific dissipation rate, and F_2 is a blending function. The calculation of the eddy viscosity remains unchanged when using the QCR formulation, while if one chooses the cubic formulation, the eddy viscosity computation is changed (STAR-CCM+, 2022).

The empirically developed Reboud correction (Reboud et al., 1998) is applied to modify the eddy viscosity in the mixture region,

$$f(\rho) = \rho_v + \left(\frac{\rho_v - \rho}{\rho_v - \rho_l}\right)^N (\rho_l - \rho_v), \tag{22}$$

where N is a constant set to the recommended value of 10. The correction for the eddy viscosity is only active in the mixture regions.

With an incompressible flow input, the segregated flow solver is selected to solve for the mass and momentum equations using the pressure-based SIMPLE algorithm for pressure-velocity coupling. Second-order convection schemes for turbulence quantities and velocity are used.

4.1. Simulation approach

Simulations were initially ran using the Moving Reference Frame (MRF) method to obtain a steady-state solution. The solution is then used to initialize the transient computations using the sliding mesh technique, referred to as Rigid Body Motion (RBM) in Star-CCM+. The time step size for the transient simulations is based on the propeller rotation rate and corresponds to 0.25 deg per time step. The computational domain is divided into a rotating region that encloses the propeller, and a stationary region for the remaining components. The rotating region is discretized using the Polyhedral and Advancing Layer Mesher (ALM) while the stationary region is meshed using the trimmer mesher, generating predominantly hexahedral cells. The boundary layer on the propeller and hub is resolved by maintaining a mean y^+ below 1.0, except for the hull and rudder at the full scale condition, where wall function is applied. The wall boundary is treated with the all-y^+ approach which incorporates blending functions for turbulent kinetic energy production and dissipation rate. Higher mesh resolution is applied in regions of expected significant pressure and velocity gradients, primarily at the fore and aft parts of the ship. To resolve the tip vortex cavitation, a control volume refinement is applied using curved cylinder shown in Fig. 4. A summary of the generated grids is provided in Table 3.

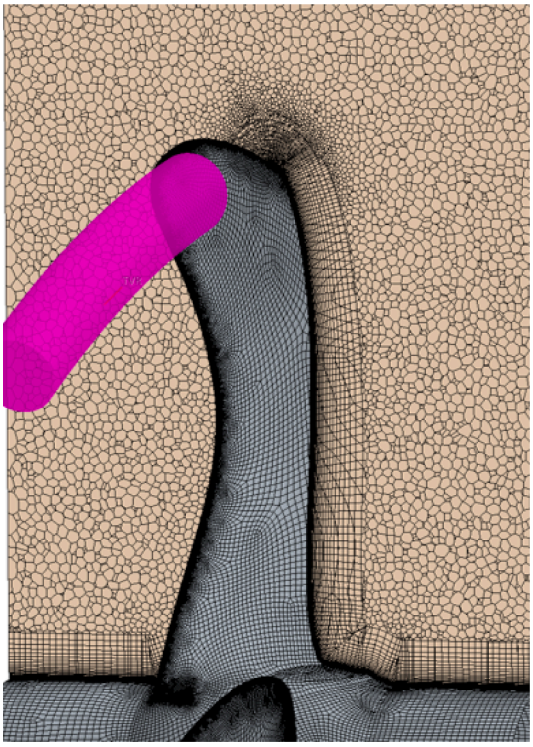

Fig. 4. Plane-cut view of generated grid for the rotating region. Cylindrical-shaped control volume to resolve tip vortex cavitation also shown.

Table 3
Summary of generated grids at model and full scale conditions.

	MS	FS
Cell count (millions)	60.9	64.5
Prism layers (propeller)	50	82
Growth ratio (propeller)	1.15	1.15
Mean y^+ (propeller)	0.34	0.083
Prism layers (Hull)	39	33
Growth ratio (Hull)	1.2	1.2
Mean y^+ (Hull)	0.54	72.2

4.2. Underwater radiated noise prediction setup

As described in Section 2, two different approaches are investigated to compute the noise emissions. First, a Permeable Data Surface (PDS) is used in combination with the FW-H acoustic analogy, and secondly the representation of the cavitation noise source through an equivalent monopole source based on cavity volume, as described in Section 2.2. The set-up of the PDS are described below, followed by a description of how the cavity volume acceleration is computed.

4.2.1. Permeable data surfaces for the FW-H method

To investigate the influence of PDS size on noise predictions, three spherical-shaped surfaces with varying sizes are created to collect flow information as shown in Fig. 5. The size of each PDS is defined relative to the propeller radius R. The largest PDS has a radius $5R$, while the medium and small surfaces are sized at $2R$ and $1.4R$, respectively. The surfaces $5R$ and $2R$ are centered at the blade tip in the 12 o'clock position, while the $1.4R$ is centered at the shaft centerline. The choice to use only spherical surfaces is based on the studies by Ge et al. (2022) and by Vikström et al. (2022), where cylindrical and rectangular permeable surfaces were shown to give rise to large errors in sound predictions from monopole sources in an incompressible computational framework. To assess the influence of PDS size, 410 receivers are placed at various lo-

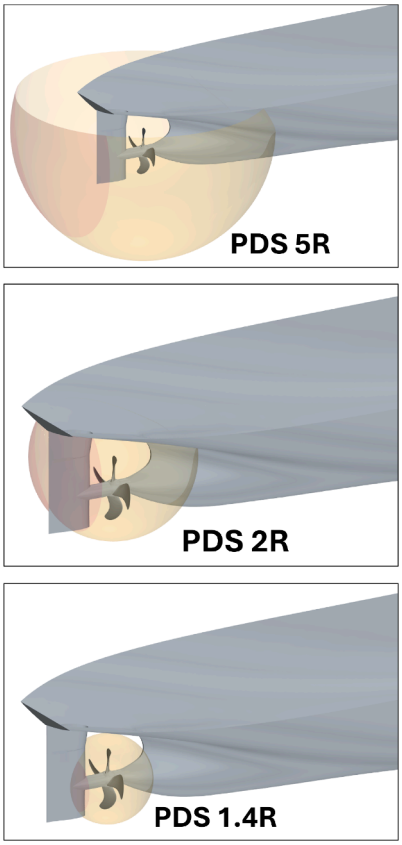

Fig. 5. Placement and sizes of the Permeable Data Surfaces (PDS) to collect flow information for the FW-H Acoustic Analogy.

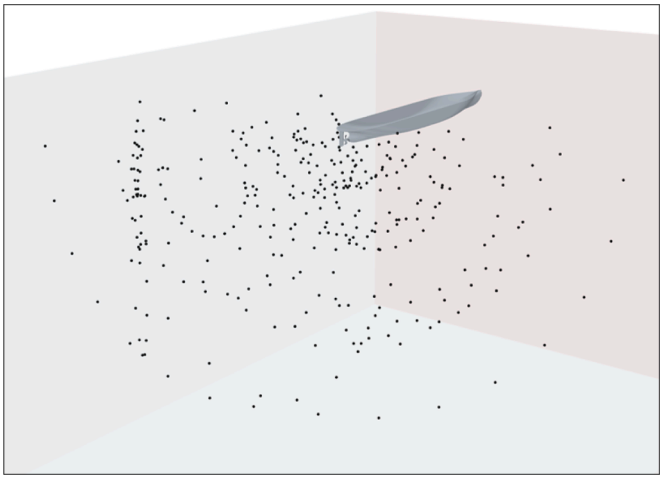

Fig. 6. Placement of 410 receivers located at various positions around the hull and propeller (some receivers are not visible in this frame).

cations on the propeller plane, upstream and downstream of it as shown in Fig. 6.

4.2.2. Computation of cavity volume acceleration

For the equivalent monopole approach, the cavity volume development needs to be computed. The cavity volume data is collected by volume integration of the vapor fraction in the domain. To compute the acoustic pressure using the correlation provided in Eq. (7), the second-order derivative of the cavitation volume over time is calculated numerically. However, as the transient volume data is collected as a discrete signal, the numerical differentiation introduces errors. These spurious distortions contaminates the resulting acoustic pressure signal, particularly at high-frequencies, therefore, the cavitation volume data must be pre-processed.

To address this contamination, an adaptation of the Locally Weighted Scatter Plot Smooth (LOWESS) (Cleveland, 1979) is applied to the collected volume data. The idea is to obtain a smooth estimation by fitting a curve while preserving the original volume signal and avoid the spurious signal introduced by the numerical differentiation.

The method processes the dataset by dividing it into segments based on user-defined input, which is typically a percentage of the total number of collected data points. In this work, the method is adapted to allow for a defined span window of data points centered around the target point. Within each segment, a linear weighted least squares regression fit is computed,

$$Y = \mathbf{X}\boldsymbol{\beta} + \epsilon, \tag{23}$$

where Y represent the smoothed dependent variable, $\mathbf{X}$ is the design matrix containing the independent variable, ϵ is the error residual, and β is the vector of regression coefficients,

$$\boldsymbol{\beta} = (\mathbf{X}^{\top}\mathbf{W}\mathbf{X})^{-1}\mathbf{X}^{\top}\mathbf{W}\mathbf{y}, \tag{24}$$

where $\mathbf{W}$ is the weighting matrix. Each data point within the span window is given a weight depending on its distance from the target point. The weighting matrix assigning the weights for each point is calculated using a tricubic function,

$$\mathbf{W} = \left[1 - \left(\frac{|x - x_o|}{d}\right)^3\right]^3, \tag{25}$$

where x is the data point to be assigned a weight, x_o is the target point, and d is the maximum distance from the target point within a span window. The tricubic weight function assigns higher weights to points closer to the target point x_o and smaller weights for those further away. By applying the local regression to each data point, a smoothed signal of the cavity volume data is obtained. An example of the resulting data is presented in Section 5.4.3.

5. Results and discussion

In this section, the influence of blockage on the wakefield distribution upstream of the propeller is first presented. Then, snapshots of the predicted cavitation pattern from the numerical simulations are compared with sketches from model scale tests. The associated predicted pressure fluctuations and pulse levels are presented and compared with data from sea trials and model tests. Following this, the applicability of the Ffowcs Williams-Hawking acoustic analogy in combination with a permeable data surface is assessed using multiple data surfaces and receiver configurations. Finally, results from the hybrid analytical-numerical approach are presented and compared with predictions from the acoustic analogy, sea trials, and model scale tests.

5.1. Blockage effect on effective wake field distribution

One of the critical steps in model scale cavitation tests is the correct simulation of the effective wake field upstream of the propeller plane. The operation of the propeller in the wake field will induce spatial and transient load variation on the blades which directly influences cavitation inception, dynamics, and pressure fluctuations. Therefore, this will play a significant role not only in the pressure pulse, but also in the underwater radiated noise levels. One of the limitations of small and medium-sized cavitation tunnels that is expected to affect the wakefield is blockage, which is defined as the ratio of the cross-sectional area of the propeller disc or hull to the test section. Due to the tunnel wall restrictions, the velocity and pressure fields around the ship model would

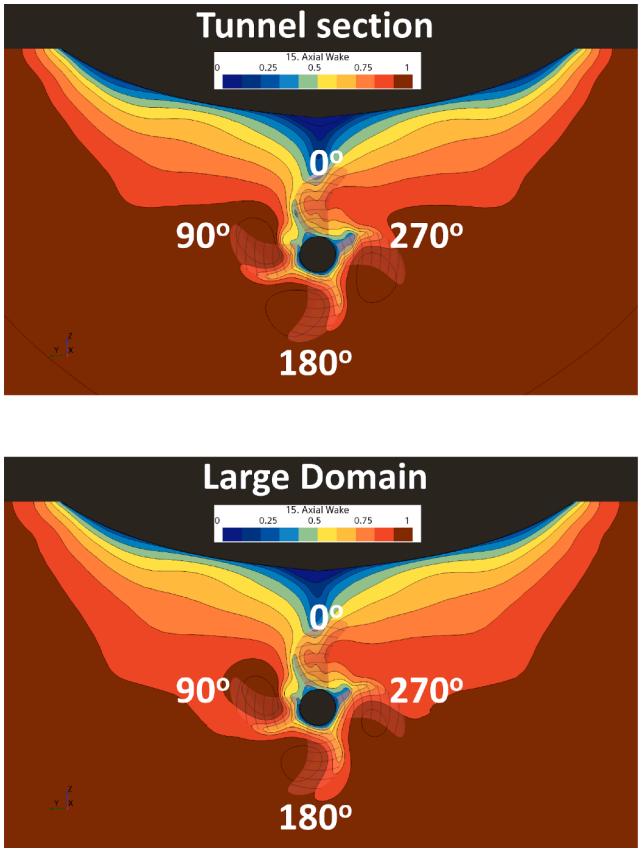

Fig. 7. Model scale axial wakefield distribution on a plane positioned at 0.19R upstream the propeller plane for Tunnel Section (top) and Large Domain (bottom).

be influenced. However, the effect of blockage on pressure fluctuations has not been systematically investigated. Therefore, this paper includes a study to investigate blockage effects on pressure pulse and underwater radiated noise levels as described in Section 3.

Fig. 7 shows numerical predictions of the axial wake on a plane located 0.19 R upstream of the propeller plane. The wakefield is significantly influenced by blockage as the velocity distribution is different between the Tunnel Section (TS) and Large Domain (LD). The restrictions from the small tunnel side and bottom walls accelerate the flow into the propeller plane which is particularly visible at the angular positions between 90^o and 270^o. The velocity distribution is also influenced at the wake peak close to 0^o, but is less visible in this plot. These variations in the wakefield influence the transient pressure distribution on the rotating propeller blades. In fact, the blades experience higher loading in the TS at the wake peak region in comparison with the LD, while the loading is lower at other angular positions, say between 90^o and 270^o. These variations will influence the cavitation volume and its dynamics, hence, affecting the pressure pulses and noise levels as discussed in subsequent sections.

5.2. Cavitation pattern

As previously mentioned, the cavitation patterns and its behavior during model-scale tests were captured using high-speed camera recordings synchronized with the shaft rotational frequency. It was observed that the cavitation behavior is highly unstable and intermittent as the shape and extent of the developed cavity at identical blade positions varied significantly with different blade passages. Similar intermittent behavior is observed for the same blade across different passages, so the intermittency is not attributed to inaccuracies with the geometry, but rather to other factors. The dynamic wakefield in the experiments significantly affects the blade loading conditions, and such variations influence cavity inception and its dynamics. Another factor is the water nuclei content which plays a significant role in the nucleation process and cavitation inception (Tani et al., 2017). Additionally, as the propeller operates at relatively low Reynolds number, the developing laminar boundary layer can restrict cavity inception, even when the local pressure falls below the vapor pressure threshold. Considering the cavity intermittency, it was concluded that comparing instantaneous snapshots from experiments with numerical predictions is not appropriate. Therefore, the sketches provided by RISE in Fig. 8 gives a better representation of the typical cavitation pattern observed during the experiments.

The numerically predicted cavitation patterns for the model scale (TS and LD) and full scale conditions are generated using an isosurface with $\alpha_v = 0.5$ and compared with experimental sketches. Full scale observations were not available due to the high turbidity during the sea trials. The patterns are shown for blade positions starting at 0^o, corresponding to the 12 o'clock position, and rotating clockwise as viewed from the upstream direction. Numerical predictions indicate that sheet cavity inception occurs slightly before the blade reaches the 12 o'clock position, though the exact inception position varies between the TS, LD, and FS conditions. While the simulations show a smooth attached sheet cavity, the experimental observations show a more intermittent pattern as indicated by dashed isolated structures. In addition, it appears that the sheet is initiated at a slightly higher position at approximately $0.85R$. The sheet continues to grow radially and tangentially before reaching its maximum volume at approximately 15^o. Nevertheless, it is limited for all conditions and is concentrated in the region above $0.9R$. However, blockage significantly affects the developed cavity as it is less extended for the LD in comparison with the TS condition. At the 20^o position, the experiments continue to show intermittent behavior while the numerical predictions show the sheet rolling and nearing collapse as the re-entrant jet approaches the blade tip. In addition, a limited tip vortex appears in the numerical simulations with varying strengths between the TS, LD, and FS conditions. The delay for the tip vortex formation in the experiments is possibly attributed to scale effects (Bosschers, 2018). At 30^o, the experiments show a smooth sheet alongside a developing small tip vortex structure. At this position, the numerical simulations show that the sheet has fully collapsed with only isolated tip vortex structures remaining. Although not visible in these snapshots, the tip vortex at model scale appears more dynamic with multiple tip bursting events in contrast to the single violent burst observed at full scale. Finally, in the experiments, the tip vortex is observed between 30^o and 40^o which is consistent with the numerical simulations.

5.3. Cavitation dynamics and pressure pulse levels

Fig. 9 shows the pressure fluctuation time history around the mean for the Ahead Transducer under cavitating flow conditions for the model scale (Tunnel Section and Large Domain) and full scale conditions. Clear differences in the pressure pulse amplitude and the time instant the peaks occur are observed for all conditions. However, no direct conclusions about scale effects are made due to the mismatch in the loading conditions between model and full scale. Comparing the TS and LD conditions shows the significant impact of blockage on the pressure fluctuations. Three major pulsating events occur during each blade passage due to the cavitation collapse. The first major pulsating event is caused by the collapse of the attached sheet cavity on the suction side as the blade exits the wake peak beyond the 20^o position. However, the collapse intensity differs significantly with a much higher peak for the TS condition. The peak of the pulsating event is delayed due to the differences in the wake region and the larger sheet cavity extent in the TS condition. The cavity extent is directly linked with pressure distribution on the suction side as the blade is more heavily loaded at this angular position in the TS resulting in a larger cavity volume and extension. After the sheet collapse, two additional pulsating events follow, which are

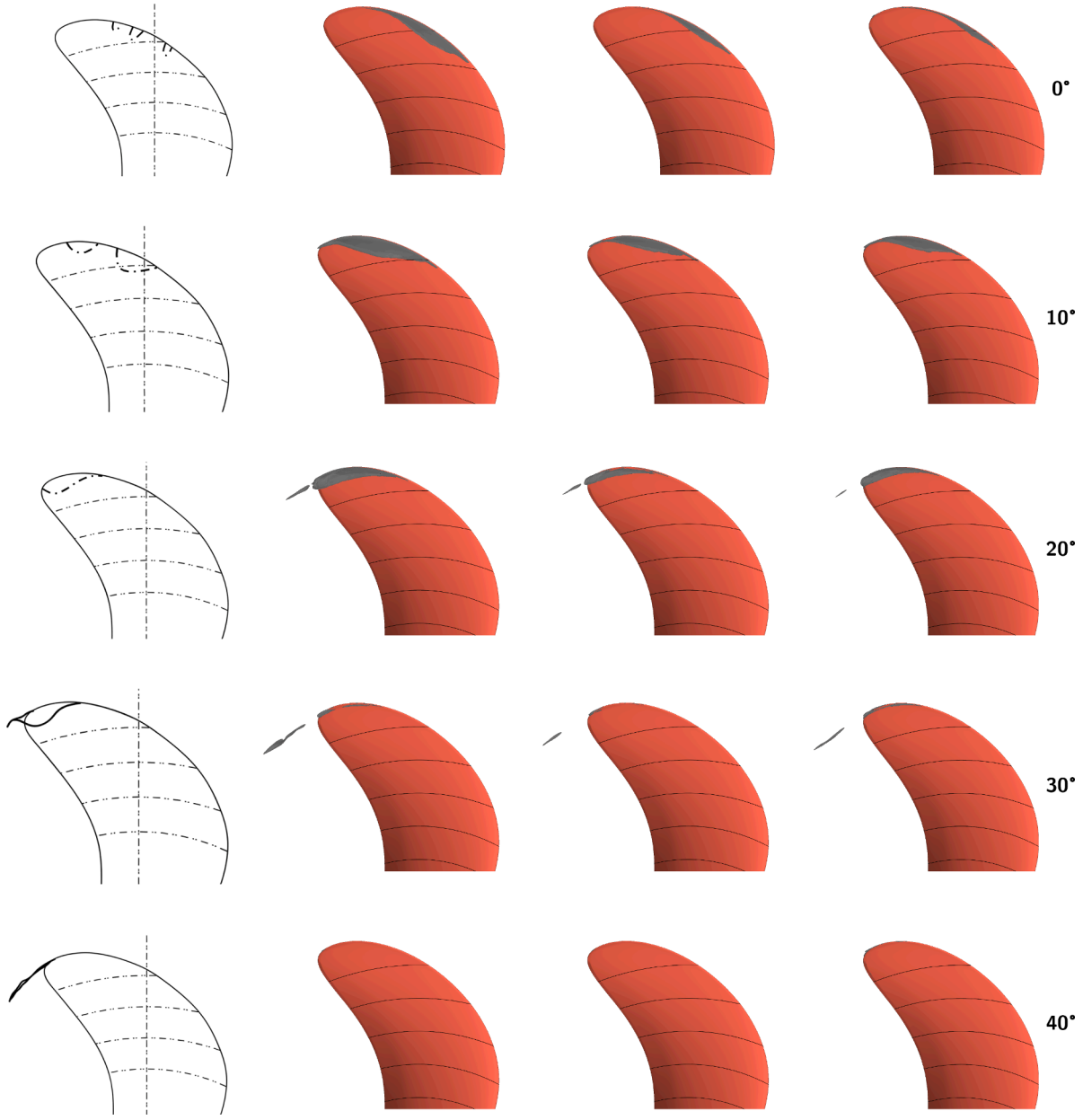

Fig. 8. cavitation patterns arranged left to right: model scale experiments, Tunnel Section (TS), Large Domain (LD), and Full Scale.

caused by the tip vortex dynamic behavior and bursting. The intensity and dynamic behavior of the tip vortex cavity also vary between the TS and LD conditions. Higher peak amplitude and delay in the bursting is observed with the TS condition. One interesting feature observed in the pressure fluctuation caused by the tip vortex for the LD condition is the appearance of a double peak at the first bursting event. This double peak is associated with the collapse of small-scale structures near the blade tip but it appears more pronounced in the signal due to the lower intensity in bursting in this condition. For the full scale condition, the cavitation dynamics is different from the model scale condition, both due to scale effects of the flow and the mismatch in the propeller loading. Similar to the model scale condition, the first pulsating event is caused by the sheet cavity collapse. However, the tip vortex is less dynamic, with a single major tip vortex bursting event observed, followed by much smaller scale fluctuations. The sudden burst of the tip vortex at full-scale conditions is likely associated with the sharp wake field gradient, but affected by diffusivity of RANS and insufficient tip vortex grid resolution.

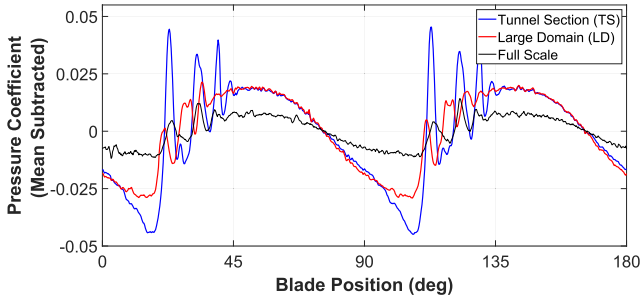

Fig. 9. Time history of induced pressure fluctuations at the Ahead transducer over two blade passages for model (including TS and LD) and full scale conditions.

The pressure pulse levels for the first four harmonic components of the Blade Pass Frequency (BPF) are shown in Fig. 10 for both the Ahead

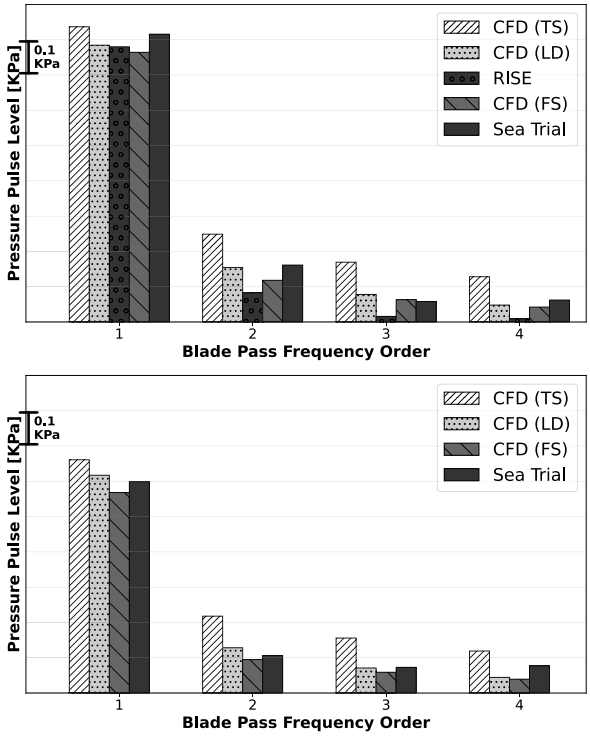

Fig. 10. Pressure pulse levels at the Ahead (top) and Astern (bottom) transducers: comparison of sea trial measurements, model scale tests, and simulation predictions.

and Astern transducers. Due to space constraints during the RISE model tests, only the Ahead Transducer was mounted. The levels are scaled using the scaling relation for the non-dimensional coefficient $K_{p(\phi)}$ which is assumed to be constant for each blade rate harmonic at both model and full scales,

$$K_{p(\phi)} = \frac{P_\phi}{0.5\rho n^2 D^2}, \tag{26}$$

where P_ϕ is the pressure amplitude at the ϕ blade rate harmonic component obtained through the Fast Fourier Transformation (FFT) , ρ is the density, n is the rotation rate, and D is the propeller diameter. Corrections for the influence of the free water surface and ship size on the pressure levels are also applied following Johnsson (1983).

For the 1st order BPF level, there is generally good agreement between the measurements and numerical predictions with a relative difference of approximately 6%. At model scale, the numerical results predict higher pressure pulse levels compared with RISE tests and full scale condition. As expected, higher levels are observed with the TS compared to the LD condition which is consistent with the variation in sheet cavitation dynamics discussed earlier. The underprediction in the RISE measurements is attributed to the intermittent cavitation behavior observed during the tests, as the results presented here are without special treatment for the intermittent behavior. When comparing the sea trial measurements with the full scale numerical results, good agreement is also found. This is an encouraging indication that the sheet cavitation dynamics, although limited in volume, has been satisfactorily captured by the numerical simulation.

Larger variations in pressure levels are observed for the higher order BPF components. Levels from the RISE measurements are significantly lower in comparison with numerical predictions and sea trials. While scale effects delay the inception of the tip vortex cavitation and hence affect the higher order pulse level, the underprediction is mainly associated with the cavitation intermittency. When comparing the sea trials with full scale numerical results, a much better agreement across all higher order components is obtained. This indicates that the tip vortex cavity formation is more consistent with each blade passage during the sea trials and as predicted by numerical results. However, the numerical predictions still generally underpredict the pressure pulse levels compared to the sea trial measurements. This is associated with the diffusive RANS approach as well as the less dynamic wakefield that leads to a weakened tip vortex bursting. Nevertheless, the results are encouraging as the numerical predictions at full scale are in good agreement with the measured data. Finally, blockage shows a significant effect on the higher order BPF components as lower levels are obtained with the LD. For completeness, Fig. 10 (bottom) shows the levels for the Astern transducer which is mounted downstream of the propeller plane. Although lower levels are observed in comparison with the Ahead transducer, similar observations are found when comparing the different conditions.

5.4. Prediction of underwater radiated noise

Predictions of underwater radiated noise levels are presented in this section. First, we demonstrate that the permeable FW-H approach may produce obviously erroneous results, thus limiting the reliability of the approach for cavitation noise predictions. Next, we compare URN measurement data with the alternative proposed approach.

5.4.1. Assessment of noise prediction levels with the permeable FW-H acoustic analogy

The purpose of this study is to further expand on the findings presented in the literature and demonstrate other limitations associated with this approach. The scope includes an assessment on the effect of PDS size, receiver placement, and end-cap effect on the underwater radiated noise levels.

Fig. 11 shows the Radiated Noise Levels (RNL) in 1/3 octave frequency bands as computed using the three spherical data surfaces for all 410 receivers. As noise levels are significantly dependent on the distance between the source and the receiver, distance normalization correction is applied assuming spherical spreading loss.

The noise levels computed from PDS 5R show a reasonable noise spectrum as expected for a cavitating propeller. The first two tonal peaks at frequencies 6.3 Hz and 12.6 Hz correspond to the first and second BPF levels. These tonal peaks are primarily dominated by the sheet cavitation noise, with a small contribution from the displaced fluid by the blade thickness in the first BPF. In addition, two humps appear at approximately 70 Hz and 100 Hz that are associated with tip vortex cavitation, followed by a drop in levels for the high-frequency broadband spectrum. Across all frequency levels, there is a significant variation/spread in the RNL for all receivers. For instance, at the first tonal peak, the RNL varies by approximately 19 dB depending on the receiver position, while a variation of about 5 dB is observed at the second tonal peak and across the broadband spectrum. Also at and above the third tonal, the spread is larger than 15 db. While a certain variation in the RNL can be associated with the directionality of the noise sources, we believe this spread is too high to be physical and thus affected by the incompressibility assumption of the fluid in the numerical prediction. Tonal RNL predictions from the smaller data surfaces $2R$ and $1.4R$ are similar to those obtained from the larger surface up to about 100 Hz. However, the noise spectrum shows a clearly unphysical behavior at higher frequencies.

To investigate and identify the source of the high frequency noise, the spectral density shown in Fig. 12 is visualized on the smallest PDS at the 1st, 2nd, and 72nd BPF. It is important to note that the surface plot scales are not uniform but are intended as a visual aid to identify the high-frequency source. Additionally, a polar directivity plot is provided for each frequency along a single radial path on the surface shown in Fig. 13. For the 1st and 2nd order BPF noise levels, the results indicate an endcap problem in the downstream direction where noticeable spikes in levels are present on the surface. This effect is clearly visible in the polar directivity plot between angular positions 135^o and 225^o for the first and second order BPF levels where sharp spikes appear on

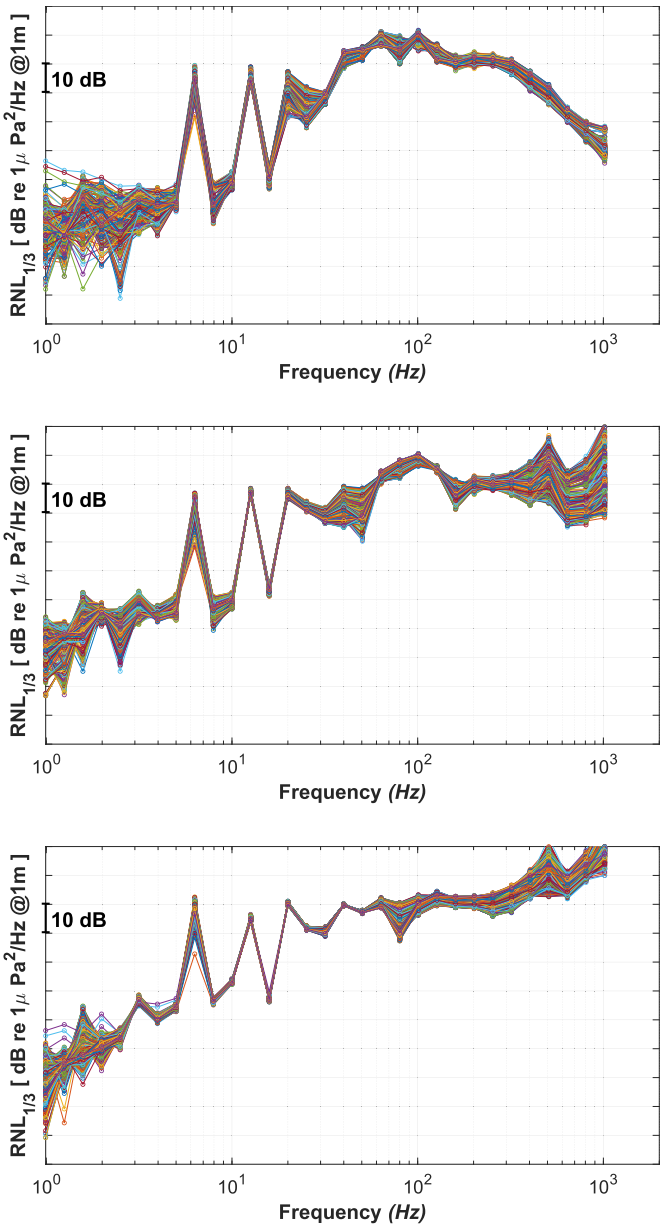

Fig. 11. Sound pressure spectral density level from varying permeable data surfaces [5R (top), 2R (middle), and 1.4R (bottom)] for all receivers. Distance normalization is applied assuming spherical spreading losses.

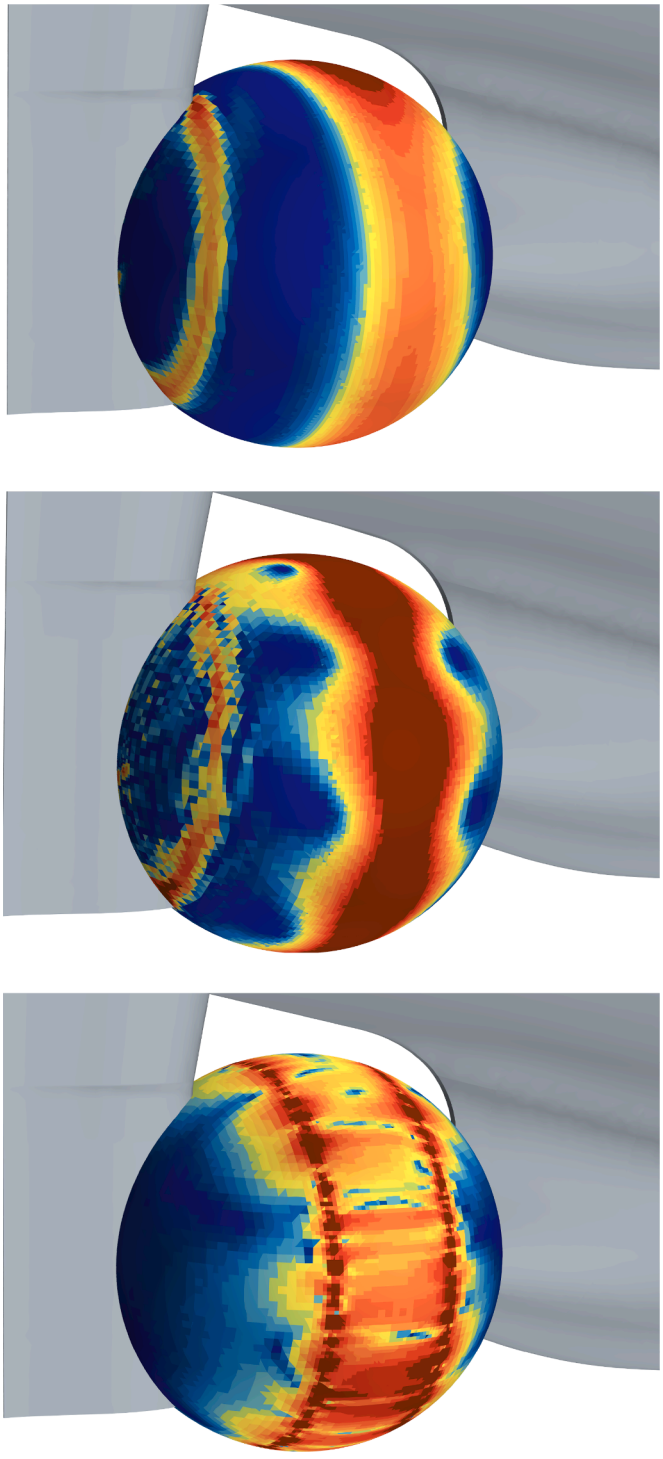

Fig. 12. Surface plot of the sound pressure level [dB/Hz] on PDS 1.4R at 1st (top),2nd (middle), and 72nd (bottom) harmonic frequencies. Important to note here that scales are not uniform.

the downstream part of the surface. Furthermore, the surface plot at frequency 453.6 Hz shows separate and sharp parallel lines with much higher noise levels. These sharp lines extend across the spherical surface and are aligned with the sharp corners of the interface connecting the rotating and stationary regions. This shows that the high frequency noise contaminating the broadband spectrum for the smaller data surfaces originates from the numerical noise introduced by the interface. As a result, unrealistically high noise levels appear in the broadband predictions. We remark that similar high frequency contamination was noted by Ge et al. (2022) for non-spherical PDS also without a rotating region; this is thus an additional effect.

To assess the influence of the end-cap effect, levels obtained by excluding the downstream portion of the permeable surface in the propeller slip are compared to those obtained using the entire surface, as shown in Fig. 14. The effect of end-cap on radiated noise levels is observed across all frequency ranges and for all three surfaces. For the first two tonal components, the radiated noise levels are reduced by approximately 5 to 10 dB when the end-cap is removed from the surface. The decrease in noise levels after end-cap removal is associated with the loss of flow information as well as the elimination of spurious noise. For the frequency levels above 30 Hz, the differences are less pronounced with variations of up to 6 dB between the total and end-cap removed computations. The results still show high frequency noise levels beyond 400 Hz for the smaller surfaces. Therefore, the end-cap effect is not a contributor to this spurious noise beyond 400 Hz.

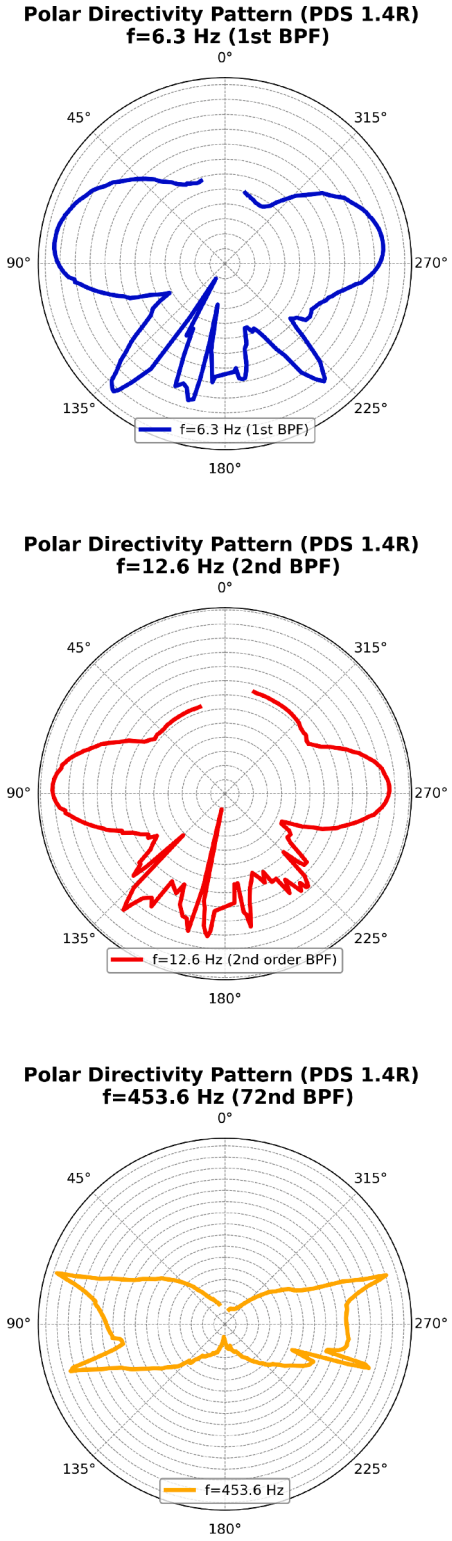

Fig. 13. Polar directivity for PDS 1.4R at 1st (top),2nd (middle), and 72nd (bottom) harmonic frequencies, taken on one radial path on the surface. Distance between radial lines represent a 4 dB difference.

All in all, the results of this study align with existing literature and show predictions of URN with the permeable Ffowcs Williams-Hawking approach can produce erroneous results. The noise levels are sensitive to the size of the permeable data surface and the position of the receivers. Although some sensitivity of noise levels to the receiver position can be attributed to natural directivity, it is also recognized that artificial directivity is introduced when this approach is combined with an incompressible flow input. The results also show that the interface connecting the rotating and stationary regions produces numerical high frequency noise that contaminates the predicted levels. Therefore, adopting a compressible flow approach to mitigate the artificial directivity problem and accurately simulate acoustic wave propagation would not resolve the issue originating from the interface. Thus a larger PDS in combination with the compressible flow approach would be needed to mitigate the erroneous effects but this would lead to an increase in computational cost due to the spatial resolution requirement for the propagating waves inside the PDS and the cost for collecting data on a larger surface. Such additional demands could be avoided by the alternative prediction method outlined in Section 5.4.3.

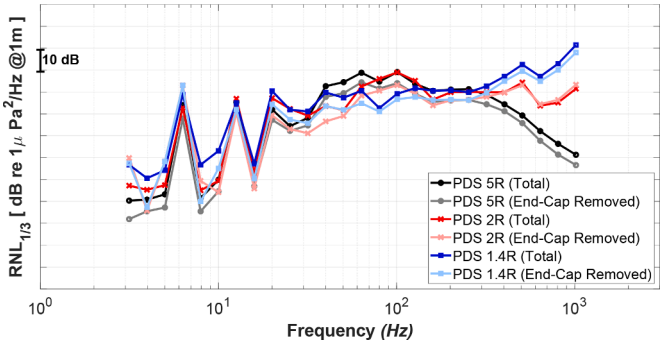

Fig. 14. Radiated noise levels from all permeable data surfaces: assessment of the end-cap on the received noise signal.

5.4.2. *Hybrid analytical-numerical approach for a cavitating propeller*

Given the limitations and challenges associated with the permeable FW-H approach for predicting URN from cavitating propellers, we here propose an alternative methodology for noise prediction. We refer to this methodology in the following as the Hybrid Analytical-Numerical Approach (A-N). The proposed method is formed by modeling the noise generation mechanism as a pulsating monopole source, as described in Section 2.2. The theoretical foundation for this is well established, as noted previously, but the application for propeller cavitation radiated noise is limited. Additionally, as described in Section 4.2, numerical differentiation of the discrete cavitation volume signal introduces artificial distortion which contaminates the acoustic pressure signal. Therefore, the cavity volume signal must be smoothed before numerical differentiation is performed to obtain the cavitation acceleration $\ddot{V}(t)$ as demonstrated in the following section.

5.4.3. *Applying LOWESS smoothing on cavity volume signal*

The total vapor/cavity volume, $V_v = \int_V \alpha_v \, dV$, is collected at each time step during the simulation over five propeller revolutions which correspond to 20 blade passages. The collected vapor data is shown by the red markers in Fig. 15 (top). The LOWESS method is applied to the collected cavity volume and the fitted curve is shown in black which captures the characteristics of the original signal with minor deviations. The bottom part of Fig. 15 shows the relative difference between the original and approximated vapor volume which are generally smaller than 2%, except for when the volume magnitude is close to zero. In addition, the root mean square error (RMSE) is approximately $8.8 \cdot 10^{-7}$. Therefore, the LOWESS fitted curve is deemed to satisfactorily maintain the characteristics of the original cavity volume signal.

The acoustic pressure shown in Fig. 16 (top) is obtained by applying the correlation expressed in Eq. (7) for both the raw cavity volume signal and the fitted LOWESS curve (smoothed). Significant high frequency fluctuations are introduced by the numerical differentiation for the raw data, while the LOWESS signal effectively removes them. The acoustic pressure signal from the smoothed cavity volume data shows two main

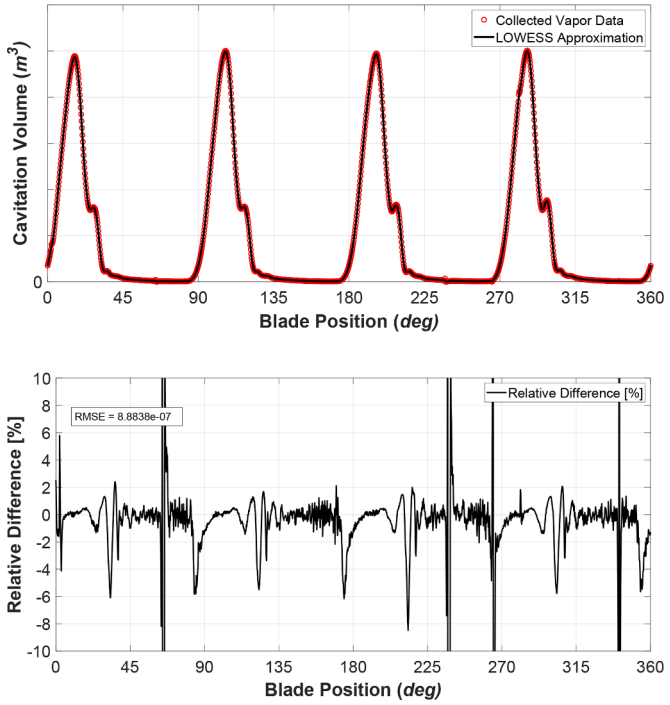

Fig. 15. Collected and approximated cavitation (vapor) volume from the simulations and approximated (smoothed) curve with the LOWESS method (Top) over four blade passages. Relative difference between the collected and approximated curves (bottom).

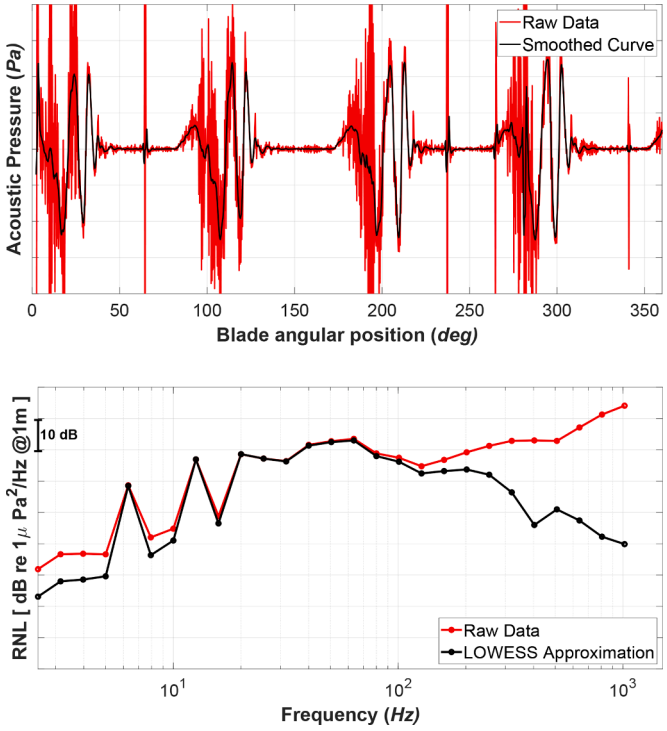

Fig. 16. Comparison of computed acoustic pressure signals from a pulsating monopole source with and without smoothing (top), and the underwater radiated noise levels (bottom).

peaks corresponding to sheet and tip vortex cavity collapses along with smaller amplitude peak, which aligns with the near-field pressure pulse signal observed in the full scale conditions. Furthermore, Fig. 16 (bottom) compares the underwater radiated noise levels with and without cavity volume smoothing applied . The results show that the signals mostly coincide in the frequency range below 100 Hz. However, the broadband levels above 100 Hz for the original signal are contaminated with spurious noise which leads to the unphysical increase in noise levels. This high frequency contamination is successfully treated through the LOWESS smoothing, resulting in a more physically reasonable noise spectrum.

5.4.4. *Comparison with model scale tests and sea trial measurements*

Results from sea trial measurements and model scale tests are presented in this section and compared with predictions from the proposed A-N approach and the FW-H acoustic analogy. For the latter the 5R PDS is used as the results from the smaller ones are polluted by the numerical errors as described above. As described earlier, the propeller pitch during the sea trials was unintentionally set to an off-design operating point. The cavitation developed on the blades was thus less extensive than initially anticipated. As a result, the underwater radiated noise levels obtained during the sea trial measurements indicate that cavitation noise is not the dominant contributor. Other radiated noise sources, such as engine noise, are prominent as well, identified via on-board accelerometer measurements. Since cavitation is not extensive at this operating condition, the model scale tests are significantly influenced by the scale effects leading to a highly intermittent behavior. Nevertheless, although the proposed approach is designed for cases where cavitation is the dominant noise source, the data remains invaluable for comparing results and identifying noise sources in each condition.

Fig. 17 shows the narrowband Source Level (SL) spectra from the sea trials, model scale tests, and full scale CFD predictions using the hybrid analytical-numerical approach. In the sea trial data shown in black, the engine was observed to dominate the low frequency noise levels. This is identified by the tonal peaks at 7.9 Hz, 9.4 Hz, and 11 Hz as they align with the harmonics of the main frequencies of the engine. This suggests that cavitation was not the dominant noise source at low frequencies, but rather that engine noise is more significant. This is further supported by the fact that these tonal peaks do not align with the Blade Passing Frequency. The model scale source noise levels from the tests are shown in blue and represent the average values from two hydrophones. The tonal components align with the BPF and are associated with the sheet cavity, but it is expected that the intermittency will reduce the levels. Additional humps are observed at 100 Hz, 500 Hz, and 700 Hz, and these broadband humps are believed to be associated with the tip vortex bursting and its dynamic behavior as well as the collapse of other small cavities. Finally, the predictions from the hybrid A-N approach are shown in red and correspond to the full scale condition. Although limited sheet and tip vortex cavitation is observed in the numerical simulations, it remains the dominant noise source in the predictions. It is important to emphasize that these predictions account exclusively for cavitation noise under free-field conditions with correction for free surface acoustic reflection. The tonal components are more pronounced here with a small hump close to 63 Hz. Moreover, peaks similar to those in the model scale measurements appear at approximately 500 Hz and 800 Hz, needless to say, there is a significant drop in levels at this frequency range.

For easier data comparison, the 1/3 octave band Source Levels are presented, computed as the power average of the 1 Hz narrowband values. Fig. 18 presents the SL data from the experimental campaigns, A-N approach, and FW-H acoustic analogy (using the 5R PDS) for the full-scale condition in 1/3 octave frequency bands. As previously discussed, sea trial tonal components and low-frequency levels (below 20 Hz) are heavily influenced by engine noise, leading to significant levels compared to model scale tests and the hybrid approach. Closer agreement is observed between the model tests and the computational predictions, though the intermittent behavior for the sheet cavitation is expected to reduce the tonal levels. A difference of approximately 10 dB still remains at the 1st BPF which is considered quite significant. More spread in the

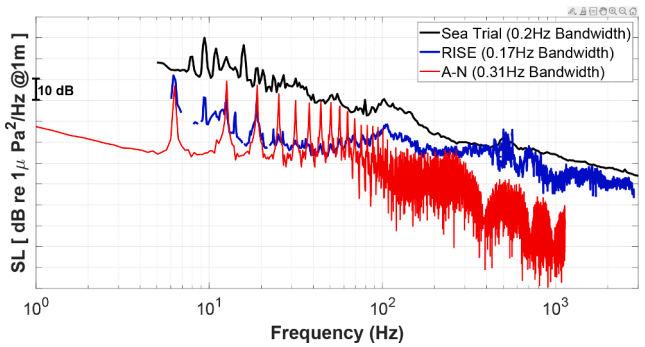

Fig. 17. Narrowband source noise levels from sea trials, model scale tests, and cavitation noise from the hybrid Analytical-Numerical (A-N) approach (at full scale condition).

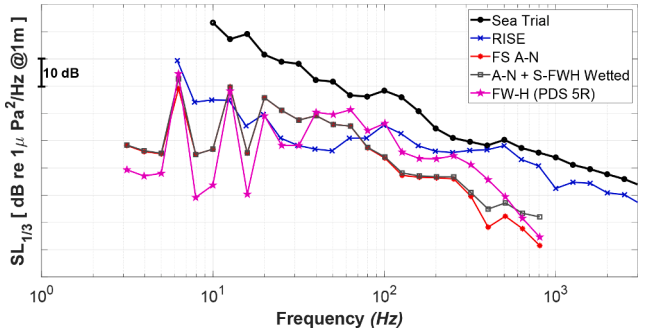

Fig. 18. 1/3 octave band source noise levels: comparison of sea trials, model scale tests, and cavitation noise from the hybrid Analytical-Numerical (A-N) approach (with and without wetted flow sources), and the PDS 5R FW-H method (full scale condition).

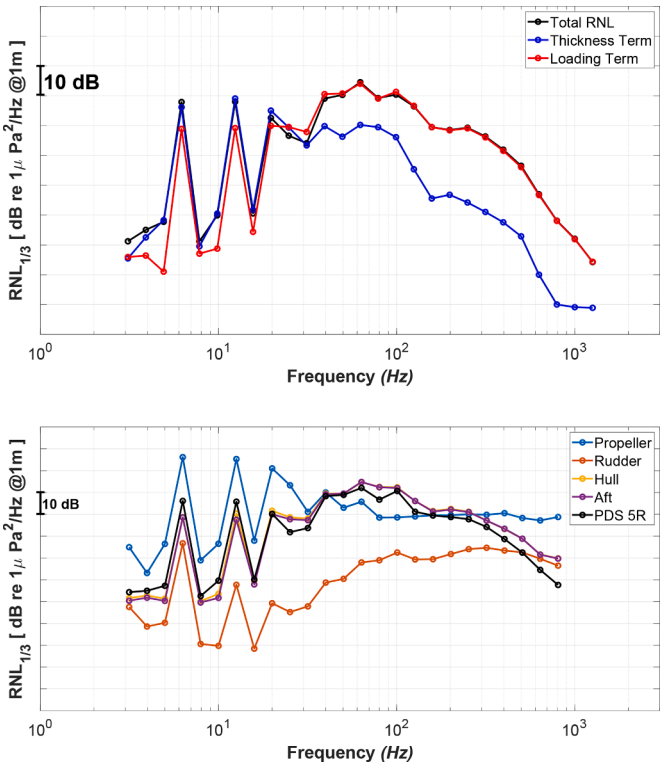

Fig. 19. Thickness and Loading terms as computed from the permeable data surface 5R (top). RNL predictions using different solid impermeable data surfaces under cavitating condition (bottom).

variations between the predictions and measurements are obtained between frequencies 20 Hz to 80 Hz. Despite considering only cavitation noise in the A-N approach, the source levels are higher than those from the model scale tests. The lower noise levels in the tests are likely due to intermittent cavitation and acoustic interference within the tunnel section. Beyond 80 Hz, the broadband spectrum shows better agreement between the measurement campaigns, while the A-N predictions show a significant drop in levels. Interestingly, the 100 Hz hump appears in the model scale and sea trial data but is not captured in the hybrid A-N approach, while the 500 Hz peak appears in all cases, but is significantly underpredicted with the A-N approach. Results obtained with the FW-H method are similar to those obtained with the A-N approach at the low frequency range. More variations are observed for the broadband spectrum with the FW-H approach showing closer levels to the measurements, especially the hump at 100 Hz which is captured by the acoustic analogy. Therefore, cavitation noise as by the A-N is not dominating the broadband spectra and further investigation on the missing broadband source is needed.

Contributions from propeller loading and thickness are not included with the A-N method. Therefore, to investigate whether the drop in the broadband levels is mainly due to the missing propeller loading term, the noise contributions from the impermeable FW-H approach for wetted flow conditions are included in combination with cavitation noise and shown in Fig. 18 in grey. The contribution from blade thickness increases the first tonal component by 3 dB, while propeller loading increases broadband levels beyond 300 Hz slightly more than that. However, this contribution is not significant enough to explain the drop in the broadband spectrum, indicating that neglecting non-cavitating flow and propeller noise is not the primary cause of this decline in levels.

To identify the missing noise source in the hybrid A-N approach, which is present in results from the FW-H acoustic analogy, the total signal from the acoustic analogy is decomposed into its thickness and loading terms as shown in Fig. 19 (top). The thickness levels indicate a similar drop off in the broadband spectrum as in the A-N approach, while the levels beyond 80 Hz are primarily from the loading term which is a dipole contribution. This suggests that the drop in the broadband levels observed with the A-N approach results from a missing dipole source. To identify dipole source, the computed noise levels from various solid impermeable surfaces under cavitating flow condition are presented in Fig. 19 (bottom). The results indicate that the increased noise levels in the broadband spectrum beyond 80 Hz and captured by the PDS originate from the hull aft surface shown in Fig. 20. This suggests that contributions from the hull should be included in the computations. This holds both for the A-N approach but needs to be considered when choosing a PDS in the FW-H approach as well. It is worth noting here that applying the FW-H acoustic analogy to the solid propeller surface where multiphase/cavitation is present is inappropriate, nevertheless, it is included in the figure for completeness. The noise levels predicted by the propeller integration surface are erroneous due to the presence of the sheet cavity on the blade surfaces. It is certainly surprising that the tonal levels are higher than predictions by the PDS, and the source of the erroneous prediction is likely due to numerical pressure disturbances from the mass transfer between the vapor (sheet cavity) and liquid phases, which are then picked up by acoustic analogy when computing the far-field predictions.

Fig. 21 shows the Source Level predictions for both model and full scale cases using the A-N approach in combination with the impermeable FW-H from the hull aft surface. When including effects from the hull surface, the broadband source level predictions are significantly improved relative to the measured levels. For example, the model scale TS condition now shows good agreement with RISE measurements for the hump at 100 Hz. However, there are still large discrepancies in broadband levels beyond 200 Hz. This drop is likely due to stronger tip vortex dynamics and more violent bursting in the experiments, as well as the

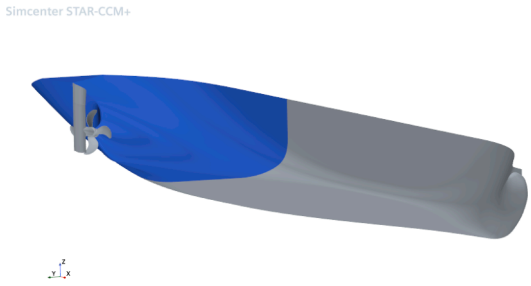

Fig. 20. Aft FW-H solid integration surface shown in blue.

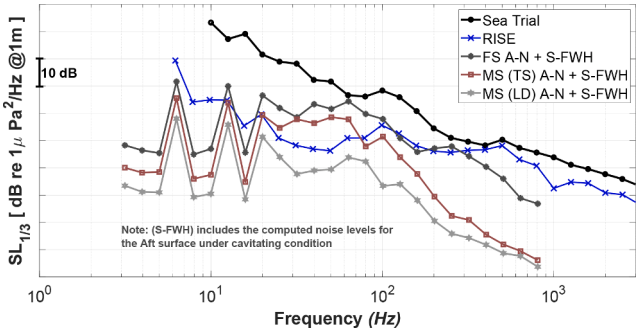

Fig. 21. Source Noise Level from experimental measurement and the hybrid A-N method for model and full scale conditions.

intermittency which will increase the broadband contribution. These events will be underpredicted with the RANS approach. Finally, predictions with the Large Domain (LD) case lead to lower Source Noise Levels across all frequencies due to the changes in cavitation volume and its dynamics as explained previously.

In summary, the hybrid analytical-numerical approach is founded in cases where cavitation is the dominant noise source, and results highlight the challenges in obtaining accurate URN prediction levels if not considering the induced pressure field on nearby surfaces. A large variation in noise levels between model and full scale measurement campaigns is observed, though some of these differences can be explained. The hybrid analytical-numerical approach shows good correlation with experimental data up to 200 Hz, but significant variations remain in the broadband levels. Further verification and comparison are needed for cases with more prominent cavitation to assess the robustness of this method.

6. Conclusion

In this paper, results on pressure pulse and underwater radiated noise (URN) levels obtained from sea trial measurements, model scale tests, and numerical predictions for a cavitating propeller operating in behind-hull conditions are presented. In addition, the blockage effect caused by the small tunnel section (TS) in model scale experiments is investigated and found to significantly influence both pressure pulse and underwater radiated noise levels compared to a larger domain (LD) section. These variations are associated with the changes in the wakefield upstream of the propeller between the TS and LD.

Regarding pressure pulse levels, good agreement between the full scale numerical simulations and sea trials is obtained for the first four blade pass frequency components. The results indicate to the capability of the numerical simulations to predict near-field pressure levels at full scale conditions. At model scale, larger discrepancies between the experiments and the numerical predictions are found, which are attributed to the intermittent cavitation behavior during the tests.

Assessment of underwater radiated noise with the permeable Ffowcs Williams-Hawkings acoustic analogy is performed with a study on its sensitivity to the integration surface size, receiver placement, and end-cap effect. It was found that smaller integration surfaces are influenced by numerical high frequency noise originating from the interface between the rotating and stationary regions. Further, the predicted Radiated Noise Level depends strongly on receiver placement, indicating non-consistent numerical results from the method.

In addition, an alternative noise prediction methodology for cavitation based on a monopole source of fluctuating volume was developed and compared against measurements at both model and full scale conditions. It was found that considering only the cavity volume dynamics is not sufficient, but also the URN originating from the induced pressure field on the hull significantly contributes. This consideration is valid when using the FW-H approach as well in assuring that the hull is enclosed by the PDS.

Large discrepancies were observed between the model experiments, the numerical predictions, and sea trial measurements. While some sources of these discrepancies have been identified, several questions remain open. The results highlight the challenges associated with URN predictions, from CFD as well as in experiments and sea trials, despite that good agreement is obtained for the near field pressure pulse levels.

CRediT authorship contribution statement

Qais Shehadeh Khraisat: Writing – review & editing, Writing – original draft, Visualization, Methodology, Investigation, Formal analysis; **Martin Persson:** Writing – review & editing, Supervision, Conceptualization; **Rickard E. Bensow:** Writing – review & editing, Supervision, Resources, Project administration, Methodology, Funding acquisition, Conceptualization.

Declaration of competing interest

The authors declare that they have no known competing financial interests or personal relationships that could have appeared to influence the work reported in this paper.

Acknowledgment

This project is funded by Kongsberg Maritime and the Swedish Transport Administration through Lighthouse Sustainable shipping program within the PUB project. The authors acknowledge Jan Hallander at RISE and Carl Andersson at IVL for the support with the experimental data from the tests performed within the PUB project. The computations were enabled by resources provided by Chalmers e-Commons at Chalmers and by the National Academic Infrastructure for Supercomputing in Sweden (NAISS) at NSC partially funded by the Swedish Research Council through grant agreement no. 2022-06725.

References

Ahmed, S., 2020. On the noise generated by a ship propeller. Ph.D. thesis. UNSW Sydney.
Aktas, B., Atlar, M., Turkmen, S., Shi, W., Sampson, R., Korkut, E., Fitzsimmons, P., 2016. Propeller cavitation noise investigations of a research vessel using medium size cavitation tunnel tests and full-scale trials. Ocean Eng. 120, 122–135. https://doi.org/10.1016/j.oceaneng.2015.12.040
Andersson, C., Linné, M., Johansson, T., Andersson, M., 2024. Measuring ship underwater radiated noise in shallow waters - why not in the near field? In: Proceedings of the Institute of Acoustics - ICUA2024. Institute of Acoustics. https://doi.org/10.25144/22211
Arveson, P.T., Vendittis, D.J., 2000. Radiated noise characteristics of a modern cargo ship. The J. Acoust. Soc. Am. 107 (1), 118–129. https://doi.org/10.1121/1.428344
Bark, G., 1985. Prediction of propeller cavitation noise from model tests and its comparison with full scale data. J. Fluids Eng. 107 (1), 112–119. https://doi.org/10.1115/1.3242424
Bensow, R., Liefvendahl, M., 2016. An acoustic analogy and scale-resolving flow simulation methodology for the prediction of propeller radiated noise. In: 31st Symposium on Naval Hydrodynamics, pp. 11–16.
Bensow, R.E., 2015. Large eddy simulation of a cavitating propeller operating in behind conditions with and without pre-swirl stators. In: Proceedings of the 4th International Symposium on Marine Propulsors, Austin, TX, USA. Vol. 4.

Borsani, J.F., Andersson, M., André, M., Azzellino, A., Bou, M., Castellote, M., Ceyrac, L., Dellong, D., Folegot, T., Hedgeland, D., Juretzek, C., Klauson, A., Leaper, R., Le Courtois, F., Liebschner, A., Maglio, A., Mueller, A., Norro, A., Novellino, A., Outinen, O., Popit, A., Prospathopoulos, A., Sigray, P., Thomsen, F., Tougaard, J., Vukadin, P., Weilgart, L., 2023. Setting EU Threshold Values for continuous underwater sound, Technical Group on Underwater Noise (TG NOISE), MSFD Common Implementation Strategy. Technical Report. Publications Office of the European Union, Luxembourg. https://doi.org/10.2760/690123

Bosschers, J., 2017. A semi-empirical method to predict broadband hull pressure fluctuations and underwater radiated noise by cavitating tip vortices. In: International Symposium on Marine Propulsors.

Bosschers, J., 2018. Propeller tip-vortex cavitation and its broadband noise. Ph.D. thesis. University of Twente.

Cianferra, M., Ianniello, S., Armenio, V., 2019. Assessment of methodologies for the solution of the ffowcs williams and hawkings equation using LES of incompressible single-phase flow around a finite-size square cylinder. Journal of Sound and Vibration 453, 1–24. https://doi.org/10.1016/j.jsv.2019.04.001

Cleveland, W.S., Robust locally weighted regression and smoothing scatterplots, J. Am. Stat. Assoc. 74 (368), (1979) 829–836.

Crighton, D.G., Ffowcs Williams, J.E., 1969. Sound generation by turbulent two-phase flow. J. Fluid Mech. 36 (3), 585–603. https://doi.org/10.1017/S0022112069001868

Curle, N., 1955. The influence of solid boundaries upon aerodynamic sound. Proc. Royal Soc. London. Series A. Math. Physical Sci. 231 (1187), 505–514. https://doi.org/10.1098/rspa.1955.0191

Directive, E.U. M. S.F., 2008. Directive 2008/56/EC of the european parliament and of the council establishing a framework for community action in the field of marine environmental policy.

Duarte, C., Chapuis, L., Collin, S., Costa, D., Devassy, R., Eguíluz, V., Erbe, C., Lamont, T., Halpern, B., Harding, H., Havlik, M.-N., Meekan, M., Merchant, N., Miksis-Olds, J., Parsons, M., Predragovic, M., Radford, A., Radford, C., Simpson, S., Juanes, F., 2021. The soundscape of the anthropocene ocean. Science 371, eaba4658. https://doi.org/10.1126/science.aba4658

Espina-Valdés, R., Fernández-Jiménez, A., Fernández Francos, J., Blanco Marigorta, E., Álvarez Álvarez, E., 2020. Small cross-flow turbine:design and testing in high blockage conditions. Energy Conv. Manag. 213, 112863. https://doi.org/10.1016/j.enconman.2020.112863

Farassat, F., 2007. Derivation of Formulations 1 and 1A of Farassat. Technical Report. NASA Langley Research Center.

Ffowcs Williams, J.E., Hawkings, D.L., 1969. Sound generation by turbulence and surfaces in arbitrary motion. Philos. Trans. Royal Soc. London. Series A, Math. Phys. Sci. 264 (1151), 321–342. https://doi.org/10.1098/rsta.1969.0031

Fischer, O., Kuthada, T., Mercker, E., Wiedemann, J., Duncan, B., 2010. CFD approach to evaluate wind-tunnel and model setup effects on aerodynamic drag and lift for detailed vehicles. Technical Report. SAE Technical Paper.

Frisk, G.V., 2012. Noiseonomics: The relationship between ambient noise levels in the sea and global economic trends. Scientific Rep. 2 (1), 437. https://doi.org/10.1038/srep00437

Ge, M., Svennberg, U., Bensow, R.E., 2020. Investigation on RANS prediction of propeller induced pressure pulses and sheet-tip cavitation interactions in behind hull condition. Ocean Eng. 209, 107503. https://doi.org/10.1016/j.oceaneng.2020.107503

Ge, M., Svennberg, U., Bensow, R.E., 2022. Investigations on prediction of ship noise using the FWH acoustic analogy with incompressible flow input. Ocean Eng. 257, 111531. https://doi.org/10.1016/j.oceaneng.2022.111531

Gray, L., Greeley, D., 1978. Source Level Model for Propeller Blade Rate Radiation for the World's Merchant Fleet. Technical Memorandum 458. Bolt Beranek and Newman, Inc.

Ianniello, S., Muscari, R., Di Mascio, A., 2013. Ship underwater noise assessment by the acoustic analogy. part i: nonlinear analysis of a marine propeller in a uniform flow. J. Marine Sci. Technol. 18, 547–570. https://doi.org/10.1007/s00466-003-0486-4

ISO 17208-1:2016, Underwater acoustics – quantities and procedures for description and measurement of underwater sound from ships: Part 1: Requirements for precision measurements in deep water used for comparison purposes, (2016).

ISO 18405:2017, Underwater acoustics – terminology, (2017).

ISO 17208-2, Underwater acoustics – quantities and procedures for description and measurement of underwater sound from ships – part 2: Determination of source levels from deep water measurements. (2019).

ITTC 7.5-02-03-03.9, 2024. Model-scale propeller cavitation noise measurement. https://www.ittc.info/media/11828/75-02-03-039.pdf.

Jalkanen, J.-P., Johansson, L., Andersson, M.H., Majamäki, E., Sigray, P., 2022. Underwater noise emissions from ships during 2014–2020. Environm. Pollution 311, 119766. https://doi.org/10.1016/j.envpol.2022.119766

Johnsson, C.A., 1983. Simple methods for first estimate of propeller induced pressure fluctuations and vibrations. In: PRADS 83. Tokyo & Seoul.

Katsuno, E.T., Dantas, J. L.D., 2022. Blockage effect influence on model-scale marine propeller performance and cavitation pattern. Appl. Ocean Res. 120, 103019. https://doi.org/10.1016/j.apor.2021.103019

Keller, J., Kumar, P., Mahesh, K., 2018. Examination of propeller sound production using large eddy simulation. Phys. Rev. Fluids 3 (6), 1–25. https://doi.org/10.1103/PhysRevFluids.3.064601

Kimmerl, J., Abdel-Maksoud, M., 2023. Visualization of underwater radiated noise in the near- and far-field of a propeller-hull configuration using CFD simulation results. J. Marine Sci. Eng. 11 (4). https://doi.org/10.3390/jmse11040834

Lafeber, F.H., Lloyd, T., Bosschers, J., 2017. Validation of underwater radiated noise predictions for a merchant vessel using full-scale measurements. In: INTER-NOISE and NOISE-CON Congress and Conference Proceedings. Vol. 255. Institute of Noise Control Engineering, pp. 3857–3866.

Li, D.-Q., Hallander, J., Johansson, T., 2018. Predicting underwater radiated noise of a full scale ship with model testing and numerical methods. Ocean Eng. 161, 121–135. https://doi.org/10.1016/j.oceaneng.2018.03.027

Lidtke, A.K., Lloyd, T., Lafeber, F.H., Bosschers, J., 2022. Predicting cavitating propeller noise in off-design conditions using scale-resolving CFD simulations. Ocean Eng. 254, 111176. https://doi.org/10.1016/j.oceaneng.2022.111176

Lighthill, M.J., 1954. On sound generated aerodynamically II. turbulence as a source of sound. Proc. Royal Soc. London. Series A. Math. Phys. Sci. 222 (1148), 1–32. https://doi.org/10.1098/rspa.1954.0049

Meng, N., Hu, X., Tian, M., 2020. Effect of blockage on critical ventilation velocity in longitudinally ventilated tunnel fires. Tunnell. Underground Space Technol. 106, 103580. https://doi.org/10.1016/j.tust.2020.103580

Menter, F.R., Kuntz, M., Langtry, R., et al., 2003. Ten years of industrial experience with the SST turbulence model. Turbulence, Heat Mass Transf. 4 (1), 625–632.

Organization, I.M., 2014. Guidelines for the reduction of underwater noise from commercial shipping to address adverse impacts on marine life.

Organization, I.M., 2023. Revised guidelines for the reduction of underwater radiated noise from shipping to address adverse impacts on marine life.

Reboud, J.L., Stutz, B., Coutier, O., Two phase flow structure of cavitation: experiment and modeling of unsteady effects, In: 3rd international symposium on cavitation CAV1998, Grenoble, France 26, (1998) 1–8.

Posa, A., Felli, M., Broglia, R., 2023. Acoustic far field of a propeller working in the wake of a hydrofoil. Phys. Fluids 35 (12). https://doi.org/10.1063/5.0176900

Salvatore, F., Ianniello, S., 2003. Preliminary results on acoustic modelling of cavitating propellers. Comput. Mech. 32, 291–300. https://doi.org/10.1007/s00466-003-0486-4

Schnerr, G.H., Sauer, J., 2001. Physical and numerical modeling of unsteady cavitation dynamics. In: Fourth international conference on multiphase flow. Vol. 1. ICMF New Orleans New Orleans, LO, USA.

Sezen, S., Atlar, M., 2023. Marine propeller underwater radiated noise prediction with the FWH acoustic analogy part 2: Assessment of model scale propeller hydroacoustic performance under non-uniform flow conditions. Ocean Eng. 270, 113443. https://doi.org/10.1016/j.oceaneng.2022.113443

Spalart, P.R., 2000. Strategies for turbulence modelling and simulations. Int. J. Heat Fluid Flow 21 (3), 252–263. https://doi.org/10.1016/S0142-727X(00)00007-2

STAR-CCM+, 2022. Simcenter STAR-CCM+ User Guide, version 2022.1.

Tani, G., Aktas, B., Viviani, M., Atlar, M., 2017. Two medium size cavitation tunnel hydroacoustic benchmark experiment comparisons as part of a round robin test campaign. Ocean Eng. 138, 179–207. https://doi.org/10.1016/j.oceaneng.2017.04.010

Tani, G., Viviani, M., Felli, M., Lafeber, F.H., Lloyd, T., Aktas, B., Atlar, M., Turkmen, S., Seol, H., Hallander, J., Sakamoto, N., 2020. Noise measurements of a cavitating propeller in different facilities: Results of the round robin test programme. Ocean Eng. 213, 107599. https://doi.org/10.1016/j.oceaneng.2020.107599

Tani, G., Viviani, M., Ferrando, M., Armelloni, E., 2019. Aspects of the measurement of the acoustic transfer function in a cavitation tunnel. Appl. Ocean Res. 87, 264–278. https://doi.org/10.1016/j.apor.2019.02.017

Testa, C., Porcacchia, F., Zaghi, S., Gennaretti, M., 2021. Study of a FWH-based permeable-surface formulation for propeller hydroacoustics. Ocean Eng. 240, 109828. https://doi.org/10.1016/j.oceaneng.2021.109828

Vikström, M., Svennberg, U., Ge, M., Bensow, R.E., 2022. The effect of porous data surface shape and size on ship noise prediction using the FWH acoustic analogy with incompressible solver for a cavitating propellers. In: Proceedings of the 7th International Symposium of Marine Propulsors.

Wang, Y., Mikkola, T., Hirdaris, S., 2022. A fast and storage-saving method for direct volumetric integration of FWH acoustic analogy. Ocean Eng. 261 (June), 112087. https://doi.org/10.1016/j.oceaneng.2022.112087

William, K., 2017. Mechanics of Flow-induced Sound and Vibration, Volume 1-General Concepts. Elsevier Science Publishing Company.